Velocity fields of N_2- and CO_2-water bubbly flows in a quasi-2D bubble column Investigation using BIV and PIV

Sarker, D.; Schinkel, C. V.; Portela, L. M.

DOI
10.1016/j.cherd.2025.10.047

Publication date
2025

Document Version
Final published version

Published in
Chemical Engineering Research and Design

Chemical Engineering Research and Design 223 (2025) 684–705

Contents lists available at ScienceDirect

Chemical Engineering Research and Design

journal homepage: www.elsevier.com/locate/cherd

Velocity fields of N_2- and CO_2-water bubbly flows in a quasi-2D bubble column: Investigation using BIV and PIV

D. Sarker [a,b,*], C.V. Schinkel [a], L.M. Portela [a]

[a] Section of Transport Phenomena, Department of Chemical Engineering, Delft University of Technology, Delft 2629 Hz, the Netherlands
[b] Department of Mechanical Engineering, International University of Business Agriculture and Technology, Dhaka 1230, Bangladesh

ARTICLE INFO

Keywords:
CO_2 Bubbly flow
Particle image velocimetry
Velocity fluctuation
Flow structure
Velocity data decomposition

ABSTRACT

This study reports the distribution of gas and liquid velocity fluctuations and flow structures in N_2-water and CO_2-water bubbly flows within a pseudo-2D bubble column reactor (BCR). PIV and BIV techniques, operating at a resolution of 750 Hz, were synchronized, and ensemble averaging of the recorded velocity fields was performed to mitigate distortions caused by light interference, reflections, and shadows. Probability density functions (PDF), power spectral density (PSD), and cross-correlation values of velocity fluctuations were calculated to analyze gas bubble interaction and dissolution in dilute to dense bubbly flow regimes. The singular value decomposition (SVD) technique was applied to correlate the flow structure distribution and energy content of velocity fluctuation. The results indicate that CO_2-water bubbly flow exhibits a bimodal distribution of velocity fluctuation at low gas superficial velocity ($U_g = 5.25 \pm 1e\text{-}4$ mm/s) due to bubble dissolution, whereas N_2-water bubbly flow at $U_g = 8.67 \pm 0.035$ mm/s shows unimodal distribution. At high gas superficial velocities ($U_g > 20.91 \pm 0.075$ mm/s for N_2 and $U_g > 15.75 \pm 0.05$ mm/s for CO_2), bubbly flows exhibit unimodal distribution of velocity fluctuations. The bimodal distribution is attributed to bubble coalescence and breakup. Experimental findings also suggest that recirculation zones near the BCR walls primarily contain small flow structures with the highest energy density and rapid structural decay. In contrast, larger flow structures are found in the center of the BCR, exhibiting slower decay. Detailed insights into CO_2 bubble dissolution could enhance BCR design, thereby improving the efficiency of relevant industrial applications.

1. Introduction

A bubble column reactor (BCR) is widely used for conducting chemical reactions in gas-liquid systems across various industries, including chemical manufacturing, petrochemicals, food processing, and steel production. Achieving efficient reactions and heat transfer requires a comprehensive understanding of mass transfer and the hydrodynamics of bubbly flows within a BCR. The hydrodynamics of bubbly flow in bubble columns are typically characterized by factors such as gas fraction distribution (Kantarci et al., 2005), gas-liquid velocity profiles (Lefebvre and Guy, 1999), and flow structures (Delnoij et al., 2000). Key parameters influencing the flow regimes in BCRs include gas superficial velocity, column aspect ratio, and the dimensions of gas injectors. For example, increasing the gas superficial velocity intensifies interactions between gas bubbles (Panicker, 2017; Medjiade et al., 2017). Various mechanisms, such as liquid flow around bubbles, bubble-bubble interactions (including bubble breakup and coalescence), significantly impact gas flow structures and liquid circulation patterns. Recent research (Sarker et al., 2023) indicates that the dissolution of gas bubbles further modifies bubble-bubble interaction mechanisms. Figs. 1a and 1b illustrate the potential effects of bubble dissolution on gas flow structures. In the case of non-dissolving N_2 bubbles, large gas fractions tend to cluster at the center of the BCR. Conversely, dissolving CO_2 bubbles result in a more homogeneous distribution of gas volume fraction, likely due to the inhibition of bubble coalescence. However, understanding the hydrodynamics of bubbly flow requires characterizing not only the gas volume fraction but also the gas and liquid velocity fields.

It is essential to separate the gas and liquid phases to determine the size of gas fractions and corresponding local gas-liquid velocities. However, phase-separated velocity measurement techniques often face challenges that can reduce accuracy. This study explores the effects of gas dissolution on gas and liquid velocity fluctuations using an innovative two-phase particle image velocimetry approach. Additionally,

* Corresponding author at: Section of Transport Phenomena, Department of Chemical Engineering, Delft University of Technology, Delft 2629 Hz, the Netherlands.
E-mail addresses: sdebasishbd@gmail.com, dsarker.me@iubat.edu (D. Sarker).

https://doi.org/10.1016/j.cherd.2025.10.047
Received 13 June 2025; Received in revised form 17 August 2025; Accepted 27 October 2025
Available online 28 October 2025

flow structures are analyzed using different methods namely Power Spectral Density (PSD), cross-correlation, and Singular Value Decomposition (SVD). The following sections review the state-of-the-art in flow characterization within bubble column reactors and techniques for gas-liquid phase separation.

1.1. Characterization of flow fields in a BCR

Many researchers (Mudde et al., 1997a; Raimundo et al., 2019) have confirmed that in a BCR, liquid rises in the center where the void fractions are higher and descends near the wall region. At low gas superficial velocities, bubble interactions are minimal; however, at intermediate gas flow rates, bubble coalescence occurs; with increasing gas flow rates, bubble breakup also takes place resulting in larger void fractions primarily in the central plume region. Generally, small bubbles move towards the wall (Besagni et al., 2023). Consequently, liquid velocities are typically higher in the middle of the BCR compared to the near-wall regions. The liquid phase circulation pattern remains largely insensitive to the exact shape of the void fraction profiles (Durst et al., 1984). The interaction between the BCR's side walls and the central wavy plume of high void fractions generates large recirculation zones, which are the dominant flow structures in the system. Additionally, small vortices with rapidly moving bubbles are observed near these larger recirculation zones, leading to a reduction in velocity fluctuations (Besbes et al., 2015; Cerqueira et al., 2018a).

Fluctuations are reported to be more pronounced in the vertical direction than in the horizontal (Alméras et al., 2016). Axial and radial liquid fluctuations exhibit anisotropic and weak directional anisotropic behaviors, respectively (Risso, 2018; Zamansky et al., 2024). For high gas fractions, the probability distribution function (PDF) of axial liquid and gas velocity fluctuations deviates from Gaussian behavior, as upward liquid fluctuations are driven by flow entrainment in bubble wakes (Prakash et al., 2016). The vertical velocity component carries nearly all the kinetic energy due to the upward motion of bubbles (Zamansky et al., 2024). In contrast, the PDF of radial liquid and gas velocity fluctuations generally follows an approximately Gaussian distribution, driven by instabilities within the bubble swarm (Risso, 2019). Due to low inertia, the gas phase tends to follow the trends of the liquid phase. The liquid/gas fluctuation may also get influenced by the direction of velocity components in the column which is not clear from the existing literature. Risso (2018) asserted that bubble-bubble interactions have minimal impact on velocity fluctuations, although there could be possibilities that these fluctuations are influenced by interfacial structures shaped by injection patterns and column geometry. On the other hand, Ruiz-Rus et al. (2022) claimed that bubble deformation and coalescence are the function of velocity fluctuation and bubble size. Nevertheless, added mass stress due to bubble dissolution may contribute to the turbulent eddies. Bubble-induced turbulence affects the interfacial mass transfer only when the eddy length scale is smaller than the equivalent bubble size (Long et al., 2022). For non-dissolving gas bubble-water system (e.g. N_2-water system), bubble coalescence and breakup govern the hydrodynamics in BCR (Leonard et al., 2021). Hosen et al. (2022) claimed that the dissolution only impacts the coalescence time.

This review highlights that, while gas fraction distribution and velocity fields in bubble columns have been extensively studied, a few works report the effects of gas dissolution on velocity fluctuations and flow structures.

1.2. Two-phase particle image velocimetry

A synchronized spatiotemporal measurement of gas and liquid phase velocities is crucial for analyzing multiphase flow dynamics. Intrusive probe techniques, however, disrupt the gas-liquid flow, leading to inaccuracies in void fraction and velocity measurements (Lau et al., 2018). Non-intrusive methods such as Laser Doppler Velocimetry (LDV), Phase Doppler Velocimetry (PDV), acoustic techniques, holography, Particle Image Velocimetry (PIV), and Particle Tracking Velocimetry (PTV) have been therefore utilized to measure void fractions and gas-liquid velocities. While PDV and LDV provide point-based measurements, they are constrained by bubble size and temporal resolution limitations (Cerqueira et al., 2018b). PIV, on the other hand, offers a comprehensive visualization, of instantaneous flow fields within a plane of the bubble column, typically from the gas sparger of a BCR to the top, over extended time periods– thus helping to unravel flow regime transition mechanisms.

A typical two-phase PIV image contains gas bubbles and tracer particles of varying sizes and shapes, with the tracer particles made visible by MIE scattering. Increasing tracer particle density can reduce measurement deviations (Liu et al., 2020) up to a limit. However, laser illumination of tracers may reflect off gas-liquid interfaces and other reflective surfaces, causing background noise from out-of-focus particles that interferes with the identification of in-focus particles. Image processing algorithms, equipped with appropriate filters, can effectively separate the gas and liquid phases in recorded PIV images (Delnoij et al., 2000; Seyfi et al., 2024; Scharnowski and Kähler, 2020). Bröder and Sommerfeld (2002), for example, enhanced image contrast by using a macro lens with a narrow focal depth (< 4 mm) and applied a combination of Laplacian of Gaussian (LoG) and median filters to isolate tracer particles and bubble contours. A combination of shadowgraphy and PIV is also commonly used to distinguish between gas and liquid phases by filtering emitted wavelengths from tracers and gas-liquid interfaces.

Merzkirch and colleagues achieved phase-separated velocity measurements in two-phase flows by employing various camera and illumination setups, such as a single CCD camera with double exposures, two synchronized CCD cameras with single exposures, and synchronized cameras with pulsed illumination (Lindken et al., 1999). They developed

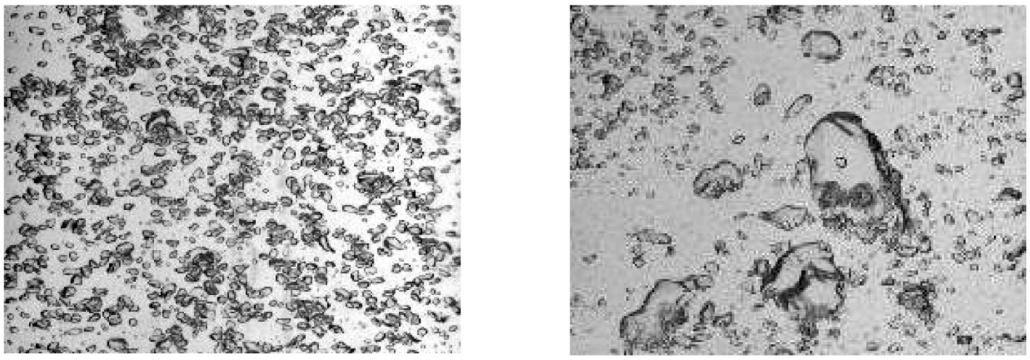

Fig. 1. Flow structures for (a) dissolving CO_2, and (b) non-dissolving N_2 bubbles.

a digital masking algorithm to differentiate continuous and dispersed phases. A challenge in PIV is that bubbles or clusters can obstruct the laser path, reducing illumination in the field of view. This leads to particularly low laser intensity on the rear sides of the bubbles, causing insufficient tracer illumination. Some researchers have used reflectors to redirect laser light, illuminating fluorescent dyes on the shaded sides of bubbles (Kim et al., 2016a). When laser light illuminates the bubble surface, it creates bright spots known as glare points, which make it difficult to distinguish and extract bubble contours from PIV images. As a solution, supplementary video cameras with backlighting are recommended to record bubble shadows (Tokuhiro et al., 1998). With laser light at 532 nm and fluorescence emissions at 585 nm, appropriate filters are employed to distinguish bubble contours from liquid dye signals, minimizing optical interference (Bröder and Sommerfeld, 2002). Table 1 summarizes the advancements in phase discrimination using shadowgraphy and PIV with fluorescent dyes. The synchronized phase discrimination method with minimizing light reflection could be an advanced solution. The present study introduces a novel phase-separated velocity measurement technique, capturing gas volume size alongside gas velocity and bubble-induced liquid velocity. By minimizing interference between LED and laser light, this method ensures high-quality measurement accuracy.

2. Experiment and data processing

2.1. Experimental setup

The experiments were conducted in a transparent pseudo-2D bubble column (990 mm×243 mm x 40 mm) containing deionized water at atmospheric pressure and room temperature, as illustrated in Fig. 2. Three sets of needle spargers were installed at the base of the bubble column, with each set comprising seven needles, each with an inner diameter of 0.8 mm. The black circles in the bottom panel with spargers in Fig. 2 indicate the three groups of needle spargers. Gas bubbles (N_2 and CO_2) were injected into the water through the spargers. The tubing, valves, and gas flow controllers were configured to allow each set of needles to inject either N_2 and CO_2 bubbles, creating three distinct gas plumes within the column. The spacing between the spargers and the gap between the sparger and the wall were carefully designed to prevent plume interactions and wall effects in the sparger region, thereby avoiding asymmetric gas distribution. We recorded PIV images and shadowgraph images of bubbles for various combinations of gas plumes, focusing on cases where all three plumes consisted solely of either N_2 or CO_2bubbles. The experiments were conducted over a sufficiently long duration, and the results were ensemble-averaged to ensure generalizability. Table 2 presents the experimental matrix for the investigation of this study. Further details regarding the experimental setup, measurement techniques, and calibration are provided in another article (Sarker et al., 2023).

A synchronized optical shadowgraphy and particle image velocimetry (PIV) setup was used to capture the bubble images and the corresponding liquid velocity field simultaneously. A high-speed video camera (1824 ×1700 pixel^2) recorded sequential images of the bubbles and the liquid velocity field with a spatial resolution of 0.42 ± 0.19 mm/pixel. A calibration plate was used to adjust the focal plane and depth of field, as well as to determine the pixel-to-length ratio. The focal distance of the camera was further fine-tuned to align with the illumination plane, optimizing the intensity of the diffracted laser light and aiding regulate particle density within the interrogation window. The camera records at a total speed of 1500 Hz. A flicker-free LED panel with a diffuser was placed behind the bubble column to ensure consistent lighting. The specifications of the PIV technique are summarized in Table 3. A laser beam, originating from an LDY304 PIV laser source, passes through a laser arm and an aperture to form a thin light sheet that illuminates the central region of the bubbly flow. This light sheet is introduced from the left side of the bubble column (Fig. 2). To verify the alignment and thickness of the light sheet, a marked paper was placed in its path.

An in-house-developed strobe controller regulated the lighting, which will be described in further detail later. The strobe controller, in combination with the PIV data processing software (DaVis 10.0.5), provided dynamic control over the LED panel and the laser light sheet (Fig. 3). This technique sequentially switches the LED panel and the laser sheet on and off to minimize light interference. When the LED panel is activated to illuminate the bubbles and a camera captures the gas-liquid interfaces, the laser light is temporarily disabled. In the following sequence, the laser illuminates the fluorescent particles, and the camera records the PIV image while the LED panel is turned off. Several studies (Kováts et al., 2018; Deckwer and Schumpe, 1993; Mudde et al., 1997b) reported that axial liquid and gas velocities can reach approximately 0.4 m/s for $u_g \approx 20$ mm/s. The PIV image capture rate is set to 750 Hz to achieve a particle shift of 2–4 pixels per frame. An exemplary graph of the pixel shift from our study is shown in Fig. A1. Moreover, the short time interval dt (1.333 ms) also allows capturing changes in bubble contours, which helps cross-correlating bubble contours and calculating the bubble displacement. At this high frequency, 100 frames of both PIV and bubble images were recorded while N_2 bubbles were injected into the BCR. For CO_2 bubbles, 50 frames were captured. After each recording sequence, there was a 10-second pause before image acquisition resumed. A recording sequence and a pause period together are depicted here as an image acquisition cycle. This process continued for 2 min for N_2 bubbles and 6 min for CO_2 bubbles. Recording pauses were introduced to accommodate the camera's memory limitations, allowing the entire dissolution period to be captured. The short exposure time of the camera, combined with the dark room environment, ensured that ambient light did not interfere with the images. A LabVIEW program controlled the mass flow controllers (MFCs) and synchronized the optical measurement techniques, ensuring that the cameras began recording a few seconds before gas injection into the column.

The solubility of CO_2 gas is significantly higher than that of N_2 gas and leads to a decrease in the *pH* of water upon dissolution, from ~7 to ~3.5. A *pH* probe (InPro 3250i SG/120, Mettler Toledo) was used to monitor the temporal evolution of *pH* in deionized (DI) water, which reflects the dissolution state of CO_2. A few grains of *NaCl* were added to water to stabilize the *pH* measurement. At high superficial gas velocities (e.g., 15.75 ± 0.05 mm/s), the *pH* changes so rapidly that the probe's response time is insufficient to capture adequate data points. Nevertheless, a trendline can be fitted to illustrate the general pattern of *pH* change.

2.2. BIV and PIV data processing

Shadowgraph images of the gas phase were analyzed using PIV-based algorithms that correlate distinct bubble contours between successive frames. The high imaging rate ensures that bubble shapes and contours change minimally between successive images, allowing accurate cross-correlation based on these unique features. This technique is referred to here as Bubble Image Velocimetry (BIV). BIV and PIV images were captured alternately using a time controller for the illumination system, both at a recording speed of 750 Hz. The odd-numbered images from odd cycles (i.e. image 1, image 3, etc. of cycle 1, cycle 3, etc.) and the even-numbered images from even cycles (i.e. image 2, image 4, etc. of cycle 2, cycle 4, etc.) constituted the BIV images. Conversely, the even-numbered images from odd cycles and the odd-numbered images from even cycles were designated as PIV images. All BIV images were grouped into a BIV subset, and all PIV images were grouped into a PIV subset for separate processing. Each set of images—BIV and PIV—underwent specific processing procedures tailored to their requirements.

Table 1
Phase-separated PIV measurements of flow regimes.

Author	FOV (pixel x pixel)	Resolution		Optics	Gas hold-up (%)	U_g (mm/s)	Remarks
		Spatial (mm/ pixel)	Temporal (Hz)				
Bröder and Sommerfeld 2002 (Bröder and Sommerfeld, 2002)	768 × 576	x - 0.1288, y- 0.2477	Gas: 5, liquid: 4	Laser illumination, interference filters (wavelength: 532 nm and 585 nm)	0.5–19	0.84–5.5	Cameras were placed in a non-perpendicular arrangement with light sheets.
Rogero et al. 2006 (Carpintero-Rogero et al., 2006)	1024 × 1024	0.49	1000	Laser and LED (643 nm) illumination, high-pass filter (570 nm)	-	-	Determination of liquid velocity was not possible in case of high number of bubbles.
Sathe at al. 2010 (Sathe et al., 2010)	2048 × 2048	0.52	1	Laser and LED (470 nm) illumination, interference filters (532 nm and 480 nm)	~5	22	Two consecutive bubble images were processed to extract a single bubble, assuming that its velocity remains constant for 4 ms.
Siddiqui et al. 2016 (Siddiqui et al., 2016)	100 × 75	~ 3	-	Laser illumination, interference filters (532 nm and 570 nm)	-	-	Intensity of the scattered light was low and a considerable amount of spurious vector was noticed in the liquid field.
Kim et al. 2016 (Kim et al., 2016b)	1280 × 800	-	270	Laser and LED (675 nm) illumination, high-pass filter (~520 nm)	0.05–0.64	3.95–24.4	A mirror was placed at the opposite wall of the bubble column to acquire a planar illumination.
Elhimer et al. 2017 (Elhimer et al., 2017)	1280 × 1024	1.56	8	Laser illumination, interference filters (532 nm and > 550 nm)	-	-	Simultaneous PIV and PTV measurements utilizing wavelength-based discrimination of light emissions from tracers and particles.
Kovats et al. 2018 (Kováts et al., 2018)	Gas: 2016 × 2016, liquid: 1376 × 1040	-	Gas: 100, liquid:6.6	Laser and halogen illumination, long pass filters (537 nm)	-	-	Shadowgraph and PIV were not synchronized.
Cerqueira et al. 2018 (Cerqueira et al., 2018a)	Gas: 1024 × 1024, liquid: 1568 × 640	-	Gas: 400, liquid: ~0.5	Laser and white LED illumination, high-band pass filter (545 nm)	2.38–19.83	-	Phase discrimination based on raw PIV images was developed.
Yan et al. 2021 (Yan et al., 2021)	20 (axial direction)	4	9	Laser illumination with beam splitter, interference filters (532 nm and 570 nm)	1	-	PIV technique is combined with endoscopic measurement. The technique records only the coordinates of tracers and particles.
Sommer et al. 2023 (Sommer et al., 2023)	1265 × 805	0.087	1000	Laser and LED illumination, optical band pass filter to block reflected laser light	5 %	2–6	A synchronized PIV and shadowgraph method was used. Both LED and laser illuminate the particles simultaneously, which may increase the chances of light interference and reflections.
Chen et al. 2024 (Chen et al., 2024)	1176 × 1768	-	-	Laser and LED illumination with mirror and image doubler, filters (640 nm, 585 nm, > 570 nm)	-	Ug: 2.55, U_l: 1650	Two-phase stereo-PIV method was employed. The image phase discrimination method is simple and suitable for 2D measurements.
Present study	1824 × 1700	0.42 ± 0.19	750	Laser and white LED illumination, long pass (540 nm) cut-off filter	20 % (max)	Ug: 5.25–26.24 (CO_2), U_g: 8.67–31.615 (N_2)	PIV and shadowgraph techniques are synchronized with an in-house developed strobe controller to prevent light interference. Bubble size, as well as gas and liquid velocities, are measured. Additionally, multiple images are ensembled, and distorted data are reconstructed to account for overlapping bubbles and laser path obstruction.

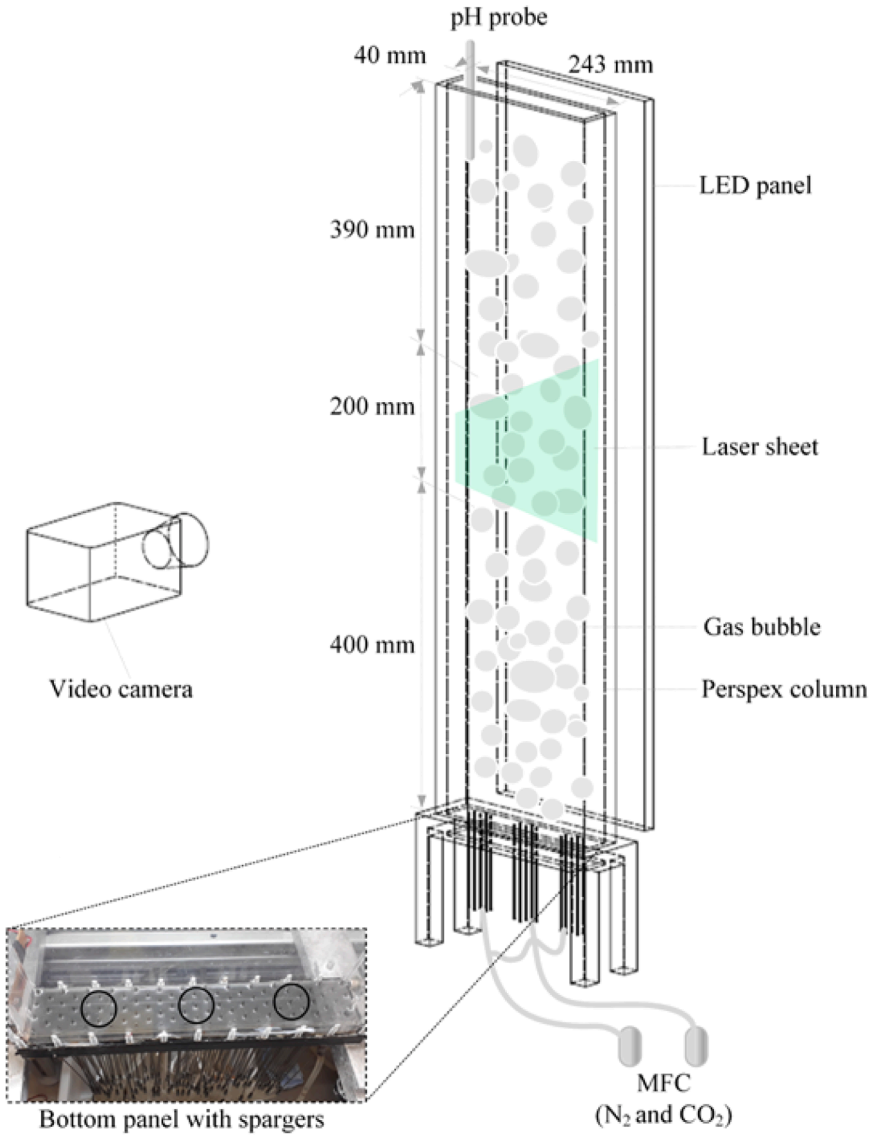

Fig. 2. A pseudo-2D bubble column with gas and liquid velocity measurement techniques (black circles represent groups of needle spargers).

Table 2
Experimental matrix.

Nos.	Gas	U_g (mm/s)	Nos.	Gas	U_g (mm/s)
1	N_2	8.67 ± 0.035	7	CO_2	5.25 ±1e−4
2		10.70 ± 0.17	8		10.50 ±1e−4
3		15.11 ± 0.076	9		15.75 ± 0.05
4		20.91 ± 0.075	10		20.99 ± 0.09
5		26.13 ± 0.61	11		26.24 ± 0.9
6		31.615 ± 0.13			

Table 3
Specifications of optical techniques.

Parameters	Settings
Camera	Imager pro HS 4 M (2016 ×2016 pixels)
Objective	AF Nikkor 28 mm and AF Nikkor 50 mm
Laser	LDY304 PIV series Pulse energy: 2 × 30 mJ Repetition rate: 0.2–20 kHz Optical power: 2x30W
Seeding particles	Fluorescent particles: PMMA-RhD, 1–20 μm

2.2.1. BIV image processing

The raw data initially displayed a bright background with dark bubble images as shown in Fig. A2a. We first inverted the images to yield bright particles against a dark background. Next, the time-averaged intensity was subtracted from each pixel to eliminate slowly varying background features, thereby enhancing the contrast of moving elements and emphasizing the bubble contours. A PIV algorithm was then applied to analyze the bubble movement and obtain velocity data. The settings for vector calculation were manually fixed. Particle displacement and time step between two consecutive integration windows were used to determine velocity. The vector processing began with an initial pass using a 128 × 128 pixel^2 window with a 1:1 square weighting and 50 % overlap to calculate a preliminary velocity field, which served as a predictor for subsequent steps. In the final step, we used a 64 × 64 pixel^2 window with 75 % overlap and applied a Gaussian weighting function, repeating this twice to refine the velocity data, ultimately yielding a vector resolution within a 16 × 16 pixel^2 window. A 75 % overlap in this case would not provide new information, only a greater number of vector. A 'universal outlier detection' median filter was applied in the multi-pass post-processing stage. This filter removed vectors with residuals greater than 2.0 and reinserted those with residuals less than 3.0, ensuring accurate and reliable velocity measurements.

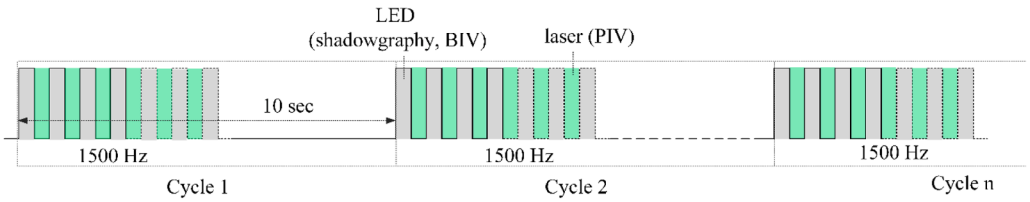

Fig. 3. A timing diagram of illumination.

2.2.2. PIV image processing

The laser sheet illuminated a section of the bubble column reactor; however, bubbles occasionally obstructed light and cast shadows, causing uneven illumination of tracer particles. A sliding minimum filter and a geometric mask were first applied to minimize bright background noise and to isolate the laser-illuminated region (Fig. A2b). Within this masked area, the maximum image intensity reached approximately 600 counts, from which 50 counts were subtracted to suppress the contribution of bubble images and highlight the PIV tracer particles. Following this, an algorithmic mask was used to isolate relevant areas of the PIV images, excluding regions without PIV particles. Subsequently, a sliding sum-of-correlation (SSOC) operation was performed with a filter length of 20 images at pyramid level 1, under the assumption of quasi-steady flow over this period (~26.67 ms). Since individual correlation maps often lacked sufficient data—particularly in regions where bubbles obstructed particle illumination and cast shadows—aggregating multiple correlation maps helped reinforce signal strength. This approach enabled more reliable identification of the maximum correlation peak. Consequently, this approach yielded 9 and 54 vector images from sets of 50 and 100 PIV images per cycle, respectively. During vector calculation, an initial pass used a window size of 64 × 64 pixel^2, which was subsequently refined to 16 × 16 pixel^2 with 50 % overlap. To eliminate erroneous vectors, a universal outlier detection (UOD) median filter was applied.

2.3. Analytical methods

PSD and cross-correlation are useful tools to predict flow structures and the deformation of structures in the flow regimes. PSD relates the energy distribution versus frequency and cross-correlation measures the similarities of structures between consecutive frames. A detailed explanation of the use of PSD and cross-correlation in BCR is available in Sarker et al. (2023).

2.3.1. Cross-correlation

Cross-correlation is a standard technique for detecting features and quantifying similarity between two signals or patterns. Here, it is used to evaluate the spatial similarity of 2D flow structures, with one pattern designated as the reference and the other as the target. The reference is compared against a sequence of target patterns over time and space; a normalized correlation value of 1 indicates identical patterns, while increasing deviations reduce the value toward a baseline. For consistent comparison across interrogation windows, gas velocities, and different gases, normalized cross-correlation is employed. This approach removes the influence of signal amplitude, yielding a dimensionless measure of linear association between patterns, ensuring that variations in velocity fluctuation patterns reflect actual flow structure changes rather than intensity differences. The MATLAB function *normxcorr2* is applied and the NCC is defined as:

$$normxcorr2 = \frac{\sum_{x,y}[I(x,y) - \bar{I}(x,y)\,]\,[I_{ref}(x+\Delta x,\quad y-\Delta y) - \quad \bar{I}_{ref}\,]}{\sqrt{\sum_{x,y}[I(x,y) - \bar{I}(x,y)\,]^2 \sum_{x,y}[I_{ref}(x+\Delta x,\quad y-\Delta y) - \quad \bar{I}_{ref}\,]^2}}.$$

where I and I_{ref} are the target and reference intensities, and $\bar{I}$ and $\bar{I}_{ref}$ are their means.

2.3.2. Singular value decomposition

The singular value decomposition (SVD) technique, introduced by (Lumley, 1967), is a foundational matrix factorization technique extensively employed in fluid mechanics to extract dominant structures and dynamic characteristics from turbulent flows. It decomposes a velocity field $u(x,t)$ or, more generally, a data matrix $\boldsymbol{M} \in R^{m\times n}$ of velocity snapshots into orthogonal spatial and temporal modes ranked by energy content. Mathematically,

$$M = U \sum V^T$$

where $\boldsymbol{U} \in R^{m\times r}$ and $\boldsymbol{V} \in R^{n\times r}$ are the left and right singular vectors (spatial and temporal modes, respectively), and $\sum \in R^{r\times r}$ is a diagonal matrix of singular values $\sigma_1 \geq \sigma_2 \geq \ldots \geq \sigma_r$. This decomposition can also be expressed for the velocity distribution as

$$u(x,t) = \sum_{k=1}^{K} a^{(k)}(t)\varnothing^{(k)}(x).$$

Here, $a^{(k)}(t)$ and $\varnothing^{(k)}(x)$ are the temporal and spatial basis functions (modes), respectively. Small-scale flow structures, containing low kinetic energy, are represented by higher modes (de Lamotte et al., 2018; Yin et al., 2019), whereas large-scale structures carrying most of the flow's energy appear in the low-order modes (Xu et al., 2020; Munir et al., 2015).

SVD is widely used for data compression, denoising, and modal analysis by projecting the flow field onto these energy-ranked bases to isolate the most energetic coherent structures while suppressing noise. A truncated reconstruction using the first $\boldsymbol{r}$ modes, $\boldsymbol{M_r} = \sum_{i=1}^{i=r} U_i\sigma_i V_i^T$, retains the essential flow dynamics. Geometrically, V^T rotates the input space to align with principal directions, Σ scales them according to their energy content, and U rotates the result into the output space. This framework not only quantifies the relative contributions of mean flow, eddies, and turbulence but also reveals possible energy disparities between gas and liquid phases due to differing velocity fluctuation magnitudes.

2.4. Uncertainties

The PIV measurements are affected by several sources of error, including bubbling, non-uniform laser power distribution, laser light reflection, and gaps in the vector field caused by obstacles. To reduce uncertainties from bubbling and background noise due to shadows, ensemble averaging of multiple experimental results is applied, along with a sliding sum-of-correlation technique. This technique enhances the correlation peak-to-background noise ratio by averaging out random background correlation noise.

Despite the application of background noise removal, spurious velocity vectors may still appear in the vector fields due to rapid variations in velocity near bubbles, image distortions at bubble edges etc. These missing or erroneous vectors are reconstructed using the Gappy-Singular Value Decomposition (Gappy-SVD) algorithm written in this study. In this process, initial gap data is generated by interpolating the surrounding values of the flawed vector. Then the PIV and BIV images were

reconstructed by SVD and determined the deviation. If the deviation is greater than a tolerance limit (tol), then the steps were iterated until the deviation $\leq$ tol. The algorithm's performance was validated by comparing a manually distorted image against the undistorted image or image that was not distorted manually. Consequently, the root-mean-square error (RMSE) of the velocity vector is kept below 0.05 for 80 % of the experiments and below 0.1 for all experiments in this study.

3. Results and discussion

3.1. Velocity fluctuation field

In this study, the PIV technique is used to capture the liquid velocity field only at the axial center of the BCR, whereas the BIV technique records the gas velocity field across the entire BCR. Gas velocity data are presented for six distinct regions, each measuring 80 × 76 mm²: A-M, A-NW, B-M, B-NW, C-M, and C-NW, as shown in Fig. 4. The vertical height of the BCR is divided into three axial segments: region A spans from 680 mm to 760 mm, region B from 440 mm to 520 mm, and region C from 200 mm to 280 mm. Laterally, the bubble column is segmented into two zones: middle (M), ranging from 77 mm to 152 mm, and northwest (NW), from 152 mm to 228 mm. The labels A, B, C, M, and NW are used to identify these regions, resulting in the following combinations: top-middle (A-M), middle-middle (B-M), bottom-middle (C-M), top-right (A-NW), middle-right (B-NW), and bottom-right (C-NW). For liquid velocity measurements, the PIV observation window is divided into a 2 × 2 array: B-M, B-NW, B'-M, and B'-NW. Here, 'B' refers to the axial segment from 520 mm to 440 mm, while 'B'' represents the region from 440 mm to 360 mm. It helps to analyze liquid velocity field against gas velocity in B-M and B-NW regions.

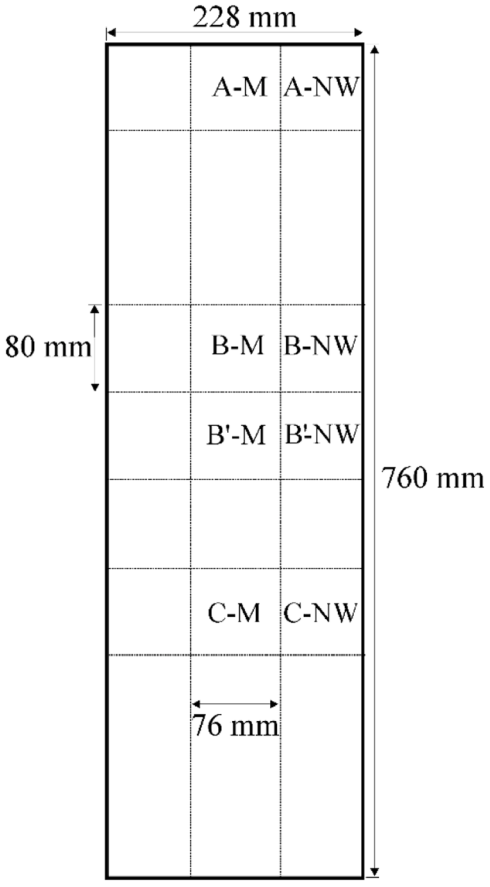

Fig. 4. Positions of the regions in the BCR.

3.1.1. Injection of N_2 gas in the water column

The gas and liquid velocity fluctuations (u'_g and u'_l) in the N_2-water system is illustrated through contour and line plots of the joint probability distribution function (PDF) in Figs. 5 and 6, respectively. To create these plots, we ensemble-averaged the velocity data within each cycle of multiple frames. The PDFs incorporate multiple variables, such as normalized velocity fluctuation, position in the bubble column, gas superficial velocity (U_g). For the CO_2-water system, 'time' is also included as a variable due to its temporal dependency. However, since the liquid velocity fluctuations in the N_2-water system do not show a significant time dependence, the 'time' variable has been omitted in those cases (see Fig. 6). The distributions of u'_g and u'_l exhibit both unimodal and bimodal behaviors: unimodal distributions peak at zero velocity fluctuation, while bimodal distributions show two symmetric peaks of equal magnitude but opposite sign (±a).

The axial and radial PDFs of N_2 gas velocity fluctuations for U_g = 8.67 ± 0.035 mm/s display an approximately Gaussian distribution at all locations within the BCR as shown in Fig. 5. As U_g increases, the PDFs become non-Gaussian, with a bi-modal distribution of u'_g observed particularly along the radial direction for U_g = 10.7 ± 0.17 mm/s and U_g = 15.11 ± 0.076 mm/s (Fig. 5a). The slope of the PDFs also decreases with increasing U_g, due to varying gas fractions resulting from bubble-bubble interactions. In the middle of the BCR, these gas fractions merge, generating both inward and outward fluctuations in the radial direction. However, the fluctuations are relatively less in the axial direction, as seen in the PDFs for U_g = 10.7 ± 0.17 mm/s and U_g = 15.11 ± 0.076 mm/s in Fig. 5b. At U_g = 20.91 ± 0.075 mm/s, the PDFs become highly asymmetric. This asymmetry in u'_{gx} diminishes as U_g rises to 26.13 ± 0.61 mm/s and 31.62 ± 0.13 mm/s. Additionally, the radial PDFs have a steeper slope than the axial PDFs, indicating that the decay of u'_g is slower in the vertical PDFs. Notably, fluctuations of equal magnitude in the axial and radial gas velocity are frequently observed near the BCR wall and center, respectively.

Fig. 6 presents the averaged liquid velocity fluctuations in the N_2-water system over multiple cycles, with shaded error bands indicating variability. The radial liquid velocity fluctuation (u'_{lx}) exhibits unimodal distribution at U_g = 8.67 ± 0.035 mm/s (Fig. 6a). For U_g of 10.7 ± 0.17 mm/s and 15.11 ± 0.076 mm/s, a bi-modal distribution appears, but as U_g increases further, the PDFs return to unimodal form. This shift suggests that the homogeneous bubbly flow transitions to a heterogeneous flow due to bubble coalescence and breakup when 8.67 ± 0.035 mm/s < U_g < 20.91 ± 0.075 mm/s in this study. Fig. 7a also confirms that the gas fractions increase and become more heterogeneous with rising U_g. At U_g> 20.91 ± 0.075 mm/s, bubble-bubble interactions become vigorous results dense bubbly flow and less variation in u'_l.

Bubble interactions and corresponding gas fractions play an important role in the distribution of u'_l. While the central portion of the PDFs remains consistent as U_g changes, the tails—vary. Pronounced multimodal fluctuations are reported laterally in the BCR's center (B'-M) and axially near-wall (B'-NW) regions, respectively. This finding implies that gas volume fractions of various sizes rise with radial liquid fluctuations at the BCR's center, while stronger liquid axial fluctuations occur near the wall as the bubbles descend. Both horizontal and vertical PDFs of u'_l exhibit symmetry, indicating that positive and negative fluctuations have comparable magnitudes. The transition of the PDFs change from wide to narrow with increasing column height (B-M, and B-NW) indicates that u'_{ly} become increasingly uniform (Fig. 6b). However, the expanded lower regions of the PDFs also reveal traces of randomness

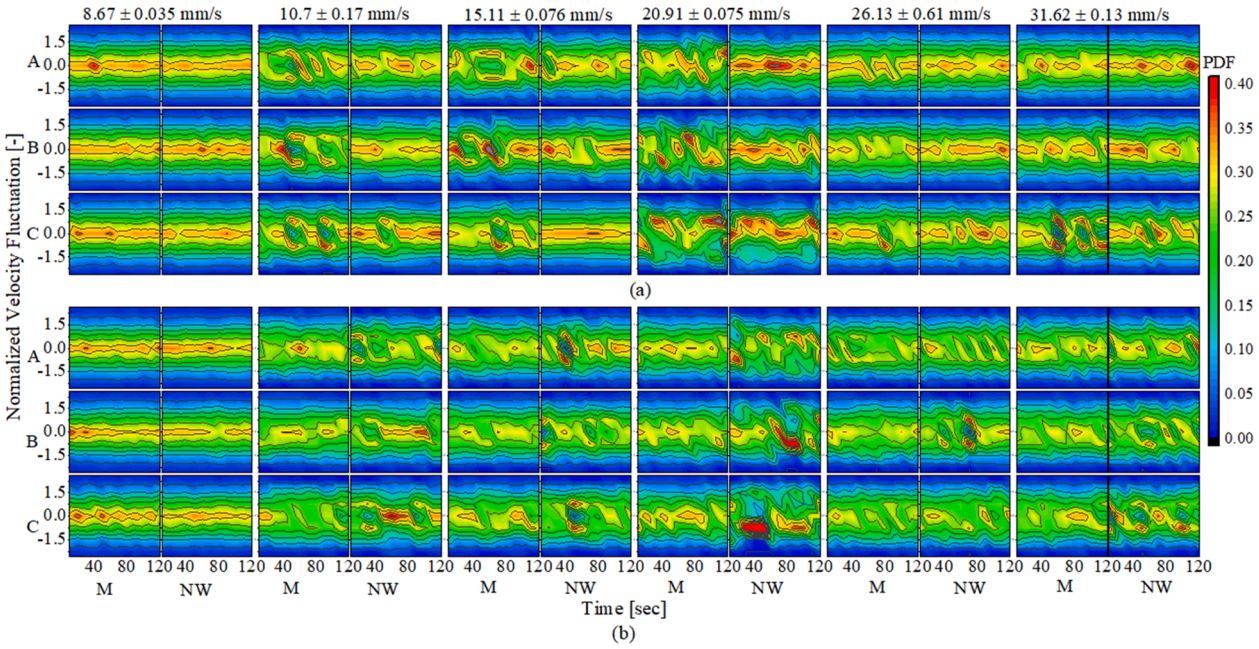

Fig. 5. Normalized radial (a), and axial (b) gas velocity fluctuation in N_2 – water system.

and the presence of recirculation zones. The steep slope of the horizontal PDFs near the BCR wall (B-NW and B'-NW in Fig. 6a) suggests that u'_{lx} in this region grow and decay more rapidly near the wall compared to the center.

Figs. 7a and 7b depict the influence of gas dissolution and bubble-bubble interactions on gas fraction distribution in the N_2– and the CO_2-water systems. In the sparger region (column height: 0–160 mm), the bubble sizes at $U_g \approx 10.50$ mm/s appear uniform in the N_2- water system but non-uniform in the CO_2–water system at 11 ms of gas injection. This indicates the presence of recirculating dissolved bubbles. At the same injection time, CO_2 bubbles rising through the middle of the column (425–525 mm) exhibit noticeable variation in bubble size distribution. However, after 6 min of CO_2 injection, dissolution approaches an asymptotic state, leading to a more uniform gas distribution both in the sparger and the mid-height of the column. In contrast, the N_2 – water system shows minimal temporal change in gas fraction; instead, the variation occurs primarily with column height. Furthermore, while clusters of uniformly sized bubbles are observed in the CO_2–water system at $U_g = 15.75 \pm 0.05$ mm/s and $U_g = 20.99 \pm 0.09$ mm/s, the N_2–water system exhibits bubble coalescence, resulting in larger gas fractions at similar U_g values. These observations suggest that CO_2 bubbles not only dissolve in water but also inhibit coalescence.

3.1.2. *Injection of CO_2 gas in the water column*

Figs. 8 and 9 present the radial and axial fluctuations of gas velocity in a bubble column with deionized water, where CO_2 gas is injected from a sparger at the bottom of the column. For each given U_g, the PDFs from multiple cycles are consolidated into a time-averaged profile, with error bounds quantifying the variability of the PDFs across cycles, as shown in Figs. 8a and 9a. The contour plots (Figs. 8b and 9b) depict only the PDFs for lower gas superficial velocities ($U_g = 5.25 \pm 1 \times 10^{-4}$ mm/s and $10.49 \pm 1 \times 10^{-4}$ mm/s). At higher superficial velocities ($U_g \geq 15.75 \pm 0.05$ mm/s), the rapid dissolution rate of CO_2 prevents capturing the time-dependent behavior of u'; hence, these cases are shown only in line plots (Figs. 8a and 9a). The solid black ($U_g = 5.25 \pm 1 \times 10^{-4}$ mm/s) and dashed gray ($U_g = 10.49 \pm 1 \times 10^{-4}$ mm/s) lines exhibit two peaks, while the colored lines display a single peak ($U_g = 15.75$–26.24 mm/s). The symmetric normal distribution with a single peak infers that gas bubbles predominantly fluctuate around fixed positions, with equal development and decay gradients of velocity fluctuations. The bimodal PDFs of u'_g also observed in some plots of CO_2-water system. It reveals the simultaneous presence of positive and negative fluctuating velocities, potentially indicating that while some bubbles fluctuate inward or upward, others move in opposite directions. Figs. 8b and 9b show that horizontal and vertical bi-modal PDFs are more pronounced in the middle (M) and near-wall (NW) regions of the bubble column reactor (BCR), decreasing in prominence as column height increases. As CO_2 gas bubbles rise and dissolve in the water, their sizes diminish gradually and it continues until the water's pH reaches an asymptotic level (pH ~ 3.5).

In line with prior studies, bubbles tend to ascend through the middle of a BCR and descend near its walls. Dissolved bubbles exhibit a strong tendency to wander, often moving toward the side walls and creating recirculation zones which confirms by Fig. 7b at $U_g = 10.49 \pm 1 \times 10^{-4}$ mm/s. The variation in bubble size due to dissolution is likely to be more noticeable in the middle and near-wall regions as the bubbles move up and down, respectively. As the flow rises the core region of the flow diffuses and recirculation zones become fade. Consequently, bubbles of uniform size appear in the upper part of the column. This behavior suggests that dissolved CO_2 gas bubbles contribute to the 1st peak of the bi-modal PDFs observed in fluctuating gas velocities. Horizontal bimodal PDFs are more prominent at $U_g = 10.49 \pm 1 \times 10^{-4}$ mm/s, particularly from the middle to the upper section of the BCR, compared to $U_g = 5.25 \pm 1 \times 10^{-4}$ mm/s. Nevertheless, bimodal PDFs for $U_g = 5.25 \pm 1 \times 10^{-4}$ mm/s are more dominant

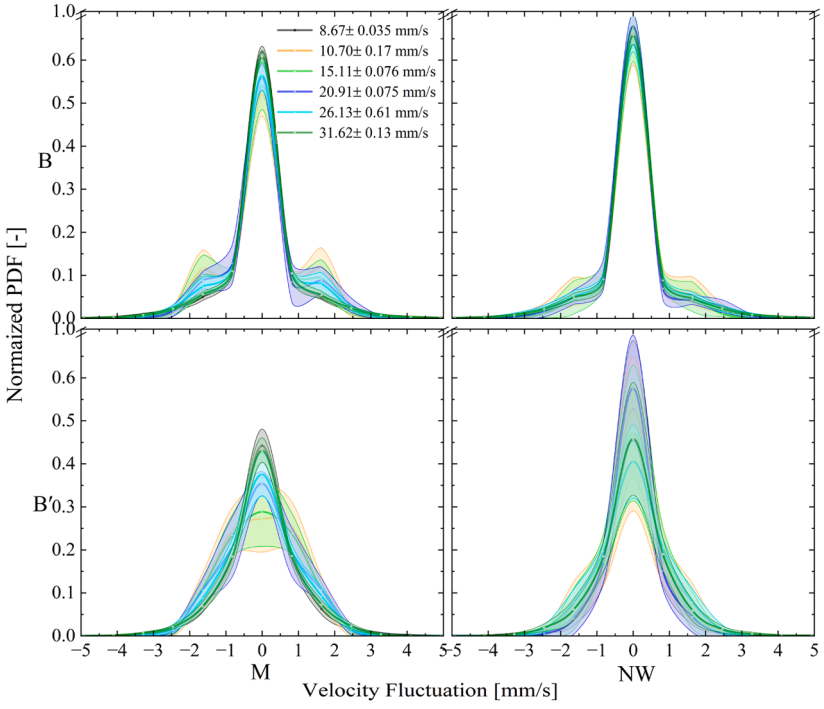

(a)

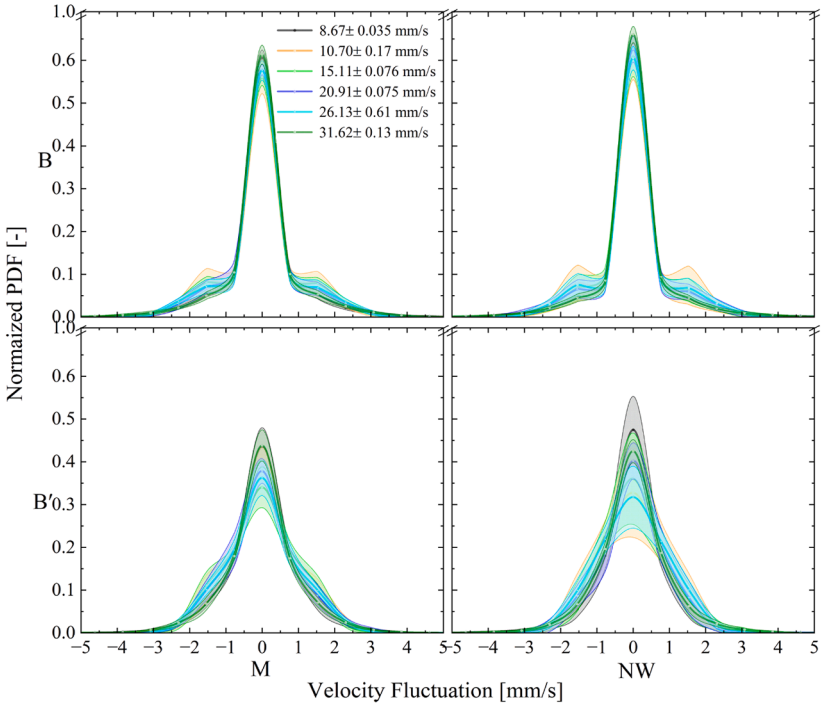

(b)

Fig. 6. Normalized PDF of radial (a), and axial (b) liquid velocity fluctuation in N_2 – water system.

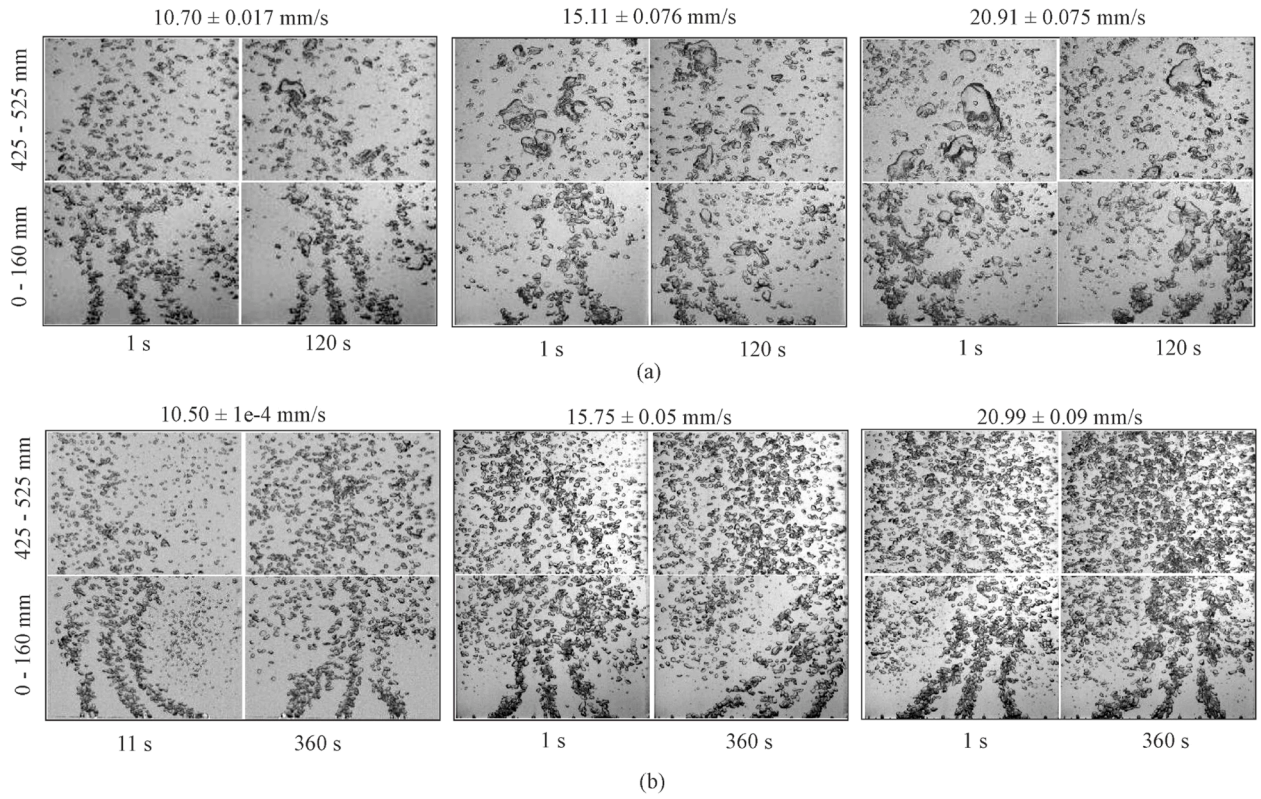

Fig. 7. Bubble images at a column height of 0–160 mm and 425–585 mm under various superficial gas velocities in (a) the N_2 –water system, and (b) the CO_2 – water system (not-scaled).

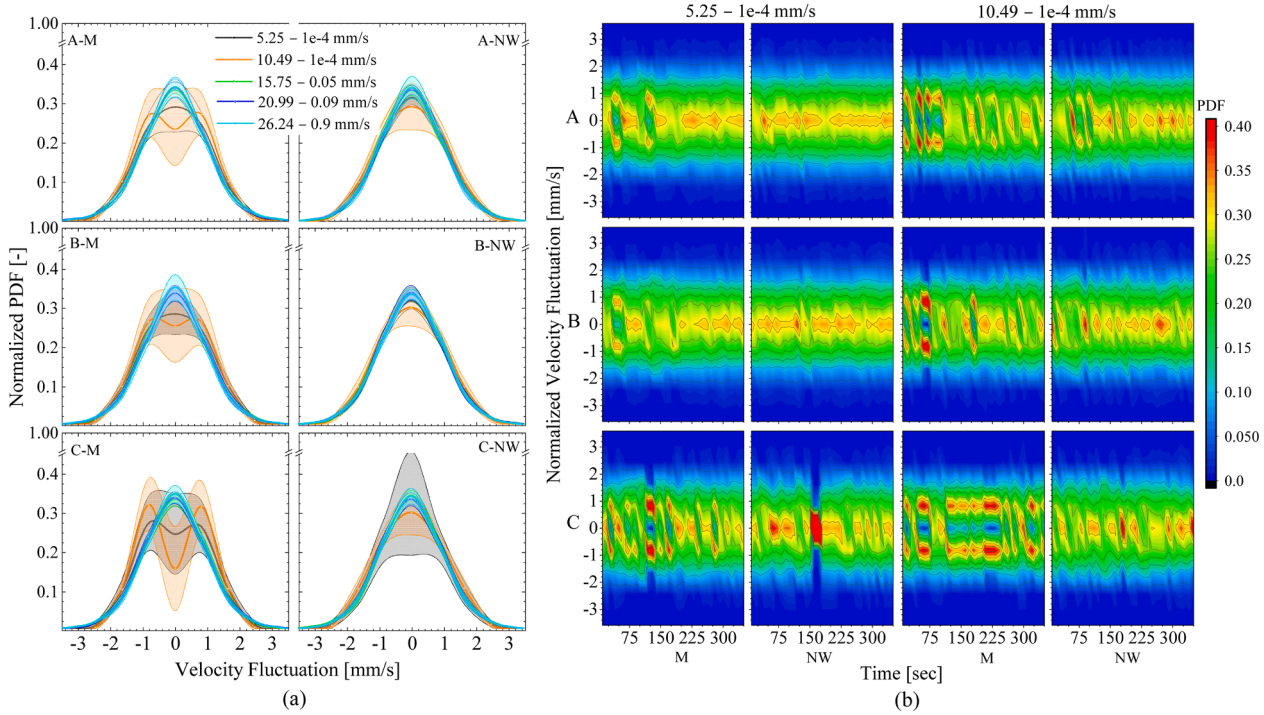

Fig. 8. Line plot (a), and contour plot (b) of normalized PDF of radial gas velocity fluctuation in CO_2 – water system.

radially at C-M and axially at B-NW and C-NW of the BCR (Fig. 9a). The bi-modal distribution transitions to unimodal as velocity increases, which explains why bi-modal PDFs for $U_g = 15.75 \pm 0.05$ mm/s are less evident in various regions.

Fig. 10 illustrates the fluctuations in liquid velocity (u_l') in the CO_2-water system, both radially and axially. At high gas superficial velocities (20.99 ± 0.09 mm/s and 26.24 ± 0.9 mm/s), both horizontal

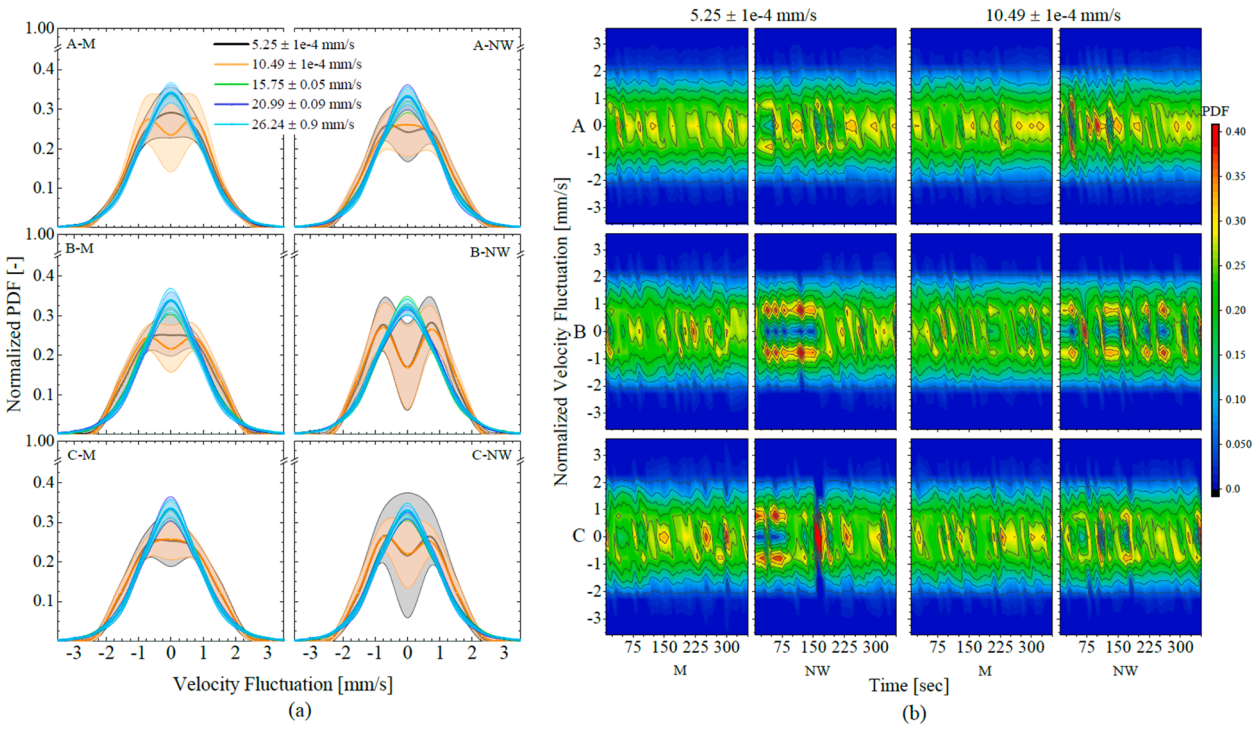

Fig. 9. Line plot (a), and contour plot (b) of normalized PDF of axial gas velocity fluctuation in CO_2 – water system.

and vertical components of u_l' exhibit unimodal normal distribution across all regions. However, at lower U_g values of 5.25 ± 1e-4 mm/s and 10.49 ± 1e-4 mm/s, the PDFs of u_l' become bimodal, with the highest probability at zero fluctuation and a secondary peak between 1 and 2.5 mm/s. The likelihood of observing this secondary peak is greater at $U_g = 10.49 \pm 1e{-}4$ mm/s than at 5.25 ± 1e-4 mm/s, and the probability of zero fluctuation is higher for high gas superficial velocities than for low ones. The dissolution of CO_2 affects bubble-induced liquid velocity over time, as reflected in the bimodal PDFs for u_l'. Figs. 9a and 9b indicate that the bimodal distribution curves for liquid velocity fluctuation are more pronounced in the middle of the BCR than near the column walls. At low U_g, vertical PDFs of u_l' from 1 mm/s to 2.5 mm/s appear dispersed in NW regions, indicating that the secondary peak in these PDFs varies with time. It also confirms that existence of axial u_l' and dissolving bubbles in NW regions of BCR.

3.2. Power spectrum of u' of N_2- and CO_2- water system

The power spectrum of velocity fluctuations reveals the energy distribution within a BCR relative to the scale of the fluctuating structures. In this study, a MATLAB code calculates the resultant velocity fluctuation ($\sqrt{u_{g,x}'^2 + u_{g,y}'^2}$) for each pixel of a recorded frame. Using the PWELCH toolbox, the one-sided spectrum and corresponding frequencies were determined. Figs. 11a and 11b illustrate the power spectra of gas velocity fluctuations in N_2- and CO_2-water systems at various positions within the BCR and for different U_g. Each curve within a window represents a cycle, as the data from multiple frames-captured at high recording speed- are averaged over time. Results for three different U_g values are shown to provide insights into dilute, intermediate, and dense bubbly flow regimes.

In all windows shown in Fig. 11a, the power spectral density (PSD) of u_g' is inversely proportional to frequency. The PSD reaches its minimum at the highest frequencies, corresponding to small-scale fluctuations and lower gas fractions. As the frequency decreases, the slope of the spectrum increases rapidly, approaching an asymptotic level around 50 Hz. The low-frequency range reflects contributions from both small- and large-scale fluctuations, with the highest energy spectra arising from agglomerated or coalesced gas fractions. Curve fitting of spectra shows two distinct slopes, $C_1 f^{-m}$ and $C_2 f^{-n}$, where f is the frequency; in most cases $m > n$. The break-point of these slopes depends on the location in BCR, u_g, and gas type. Similarly, Risso (2018) reported a power spectral curve with a decreasing slope at higher frequencies, although his study did not identify any location-dependent effects within a BCR. Fig. 11a indicates that the influence of large structures is relatively less pronounced in the NW windows. Since the gas plume ascends through the center of the BCR while smaller-scale fluctuations dominate near the wall, the velocity fluctuations in the BCR center transfer more energy at low frequencies than near the wall for any U_g (Fig. 11a). This observation is consistent with Deshpande et al. (2010), who reported higher power density at large frequencies in the NW regions compared to the bulk region. Additionally, the energy contributions at low frequencies tend to increase with column height, while the slope differences between middle and near-wall regions inversely correlate with U_g. It refers that the contributions of large-scale structures to energy density reduce gradually with U_g.

In contrast, CO_2-water system exhibits greater energy spectra in NW windows than in M windows (Fig. 11b). In the N_2-water system's M windows, power densities are higher than those in the CO_2-water system. Moreover, Fig. 11b also illustrates that the energy spectra of

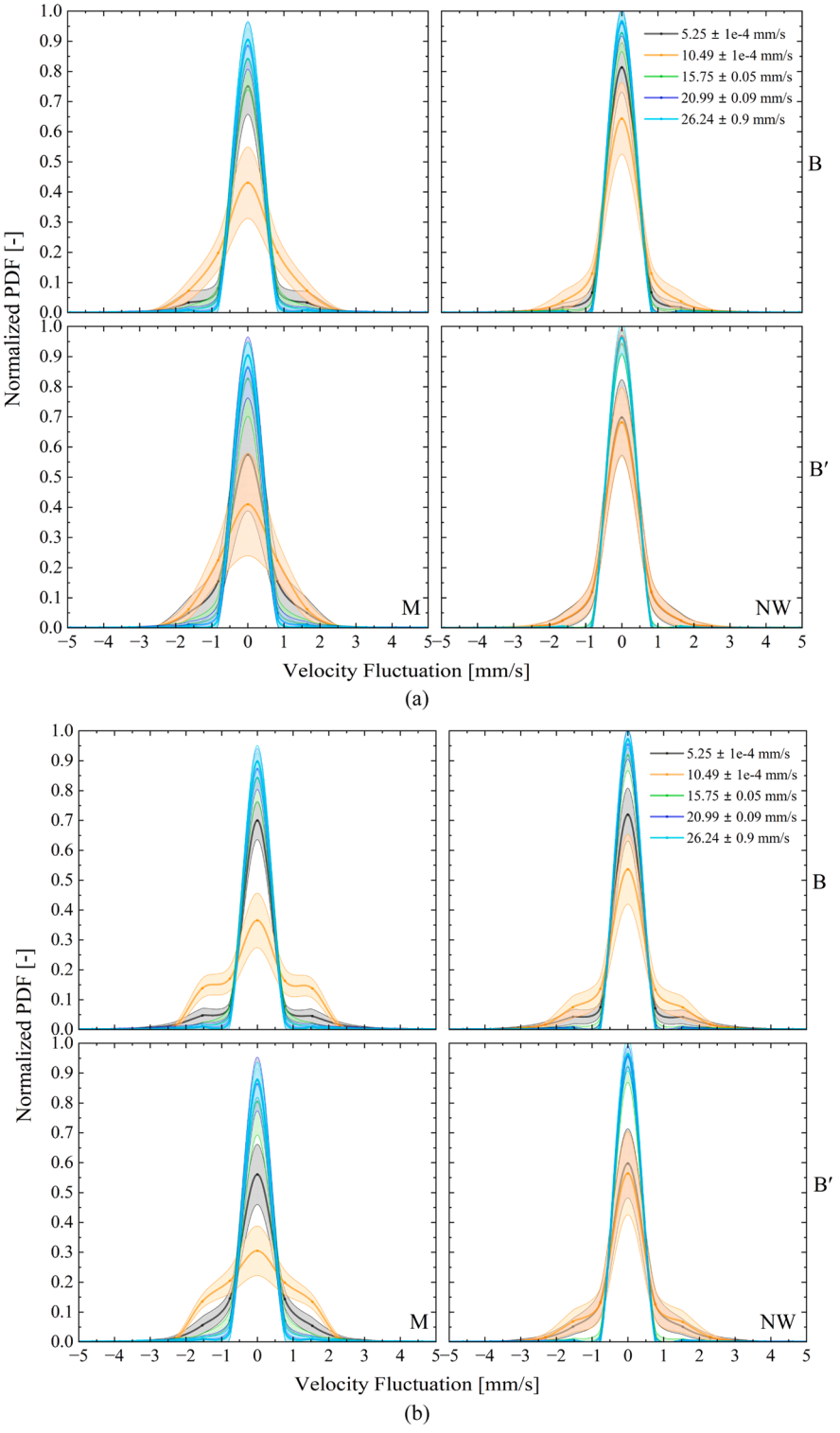

Fig. 10. Normalized PDF of radial (a), and axial (b) liquid velocity fluctuation in CO_2 – water system.

multiple cycles in the near-wall windows converge with increasing column height, indicating a dominant influence of small-sized gas and velocity fluctuations throughout the bubbling period, with minimal contributions from larger fluctuations. In M windows, energy spectra curves reach to the asymptotic level at close to 100 Hz. Hence, fluctuations with greater than 100 Hz have very less contributions to the energy spectra. This again indicates the dominance of small-scale structures in the CO_2-water system. However, the energy spectra curve shape in the CO_2-water system's M windows resemble that of the N_2-water system, suggesting substantial influence from large-scale velocity fluctuations. In the CO_2-water system, as U_g increases, the entire energy spectrum in the BCR center shifts upward due to the presence of numerous agglomerated small bubbles. As the gas bubbles ascend, gas dissolution effects weaken, and recirculation zones decrease, amplifying the influence of small-scale fluctuations even in NW windows. Consequently, when the gas plume reaches the A-NW windows, the energy spectra across different gas velocities become nearly identical.

Additionally, the cycle-wise PSD curves reveal the temporal stability

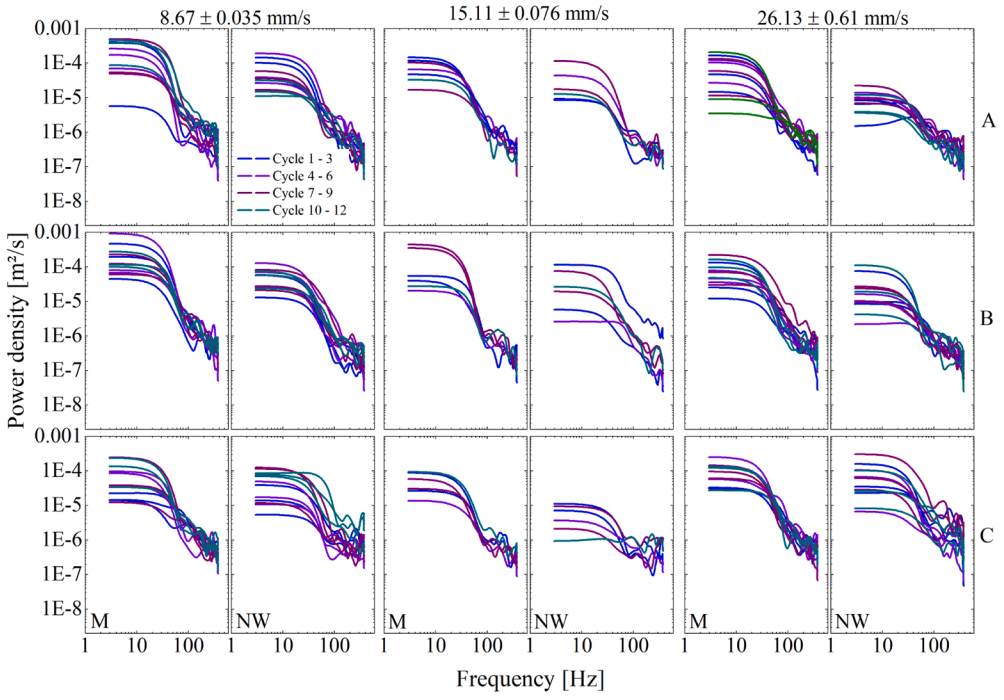

(a)

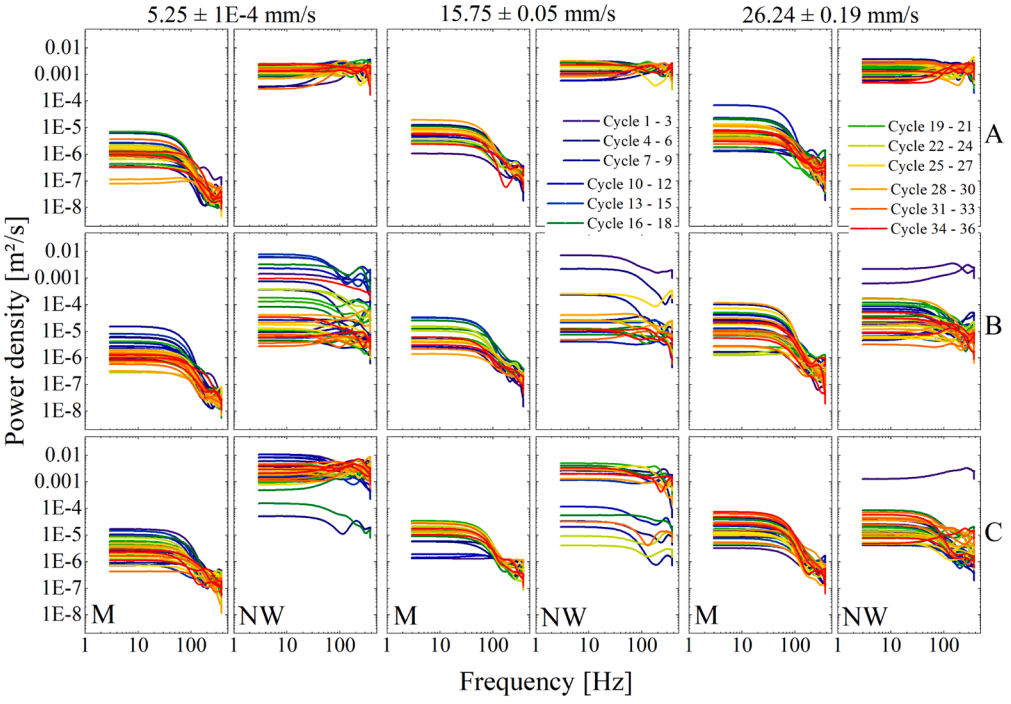

(b)

Fig. 11. Power spectral density of N_2 (a), CO_2 (b) gas velocity fluctuation.

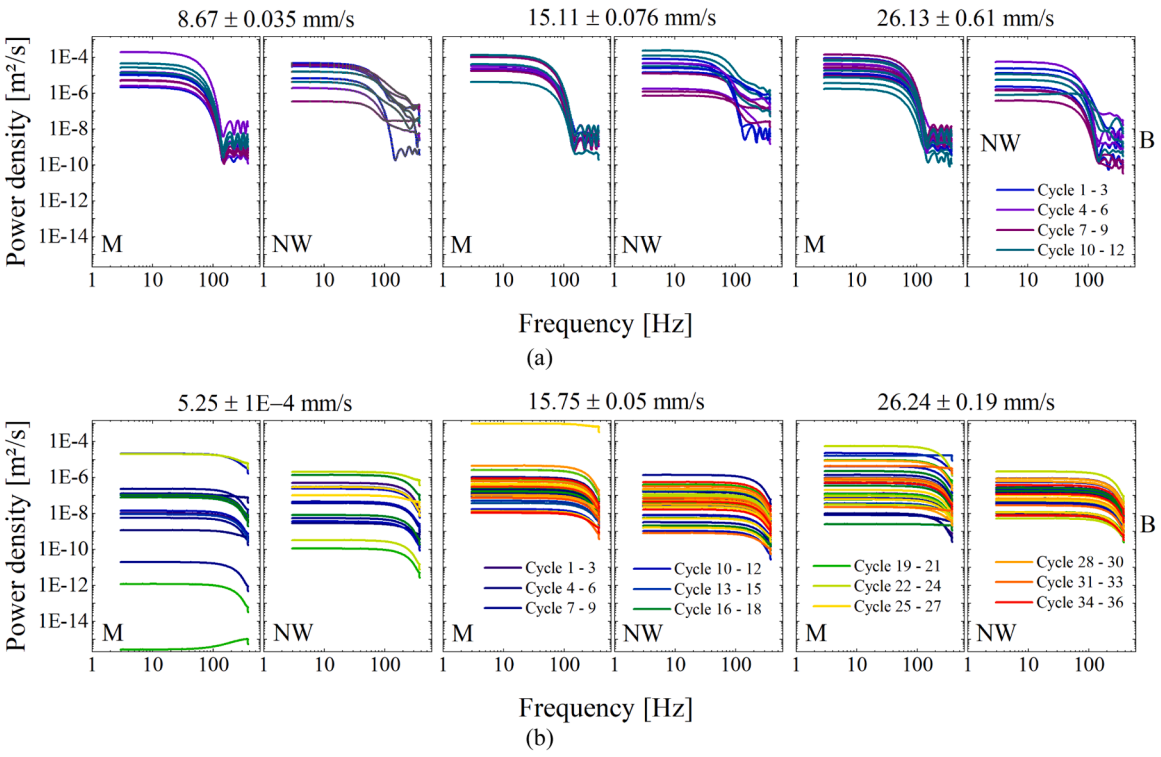

Fig. 12. Power spectral density of N_2 (a), CO_2 (b) liquid velocity fluctuation.

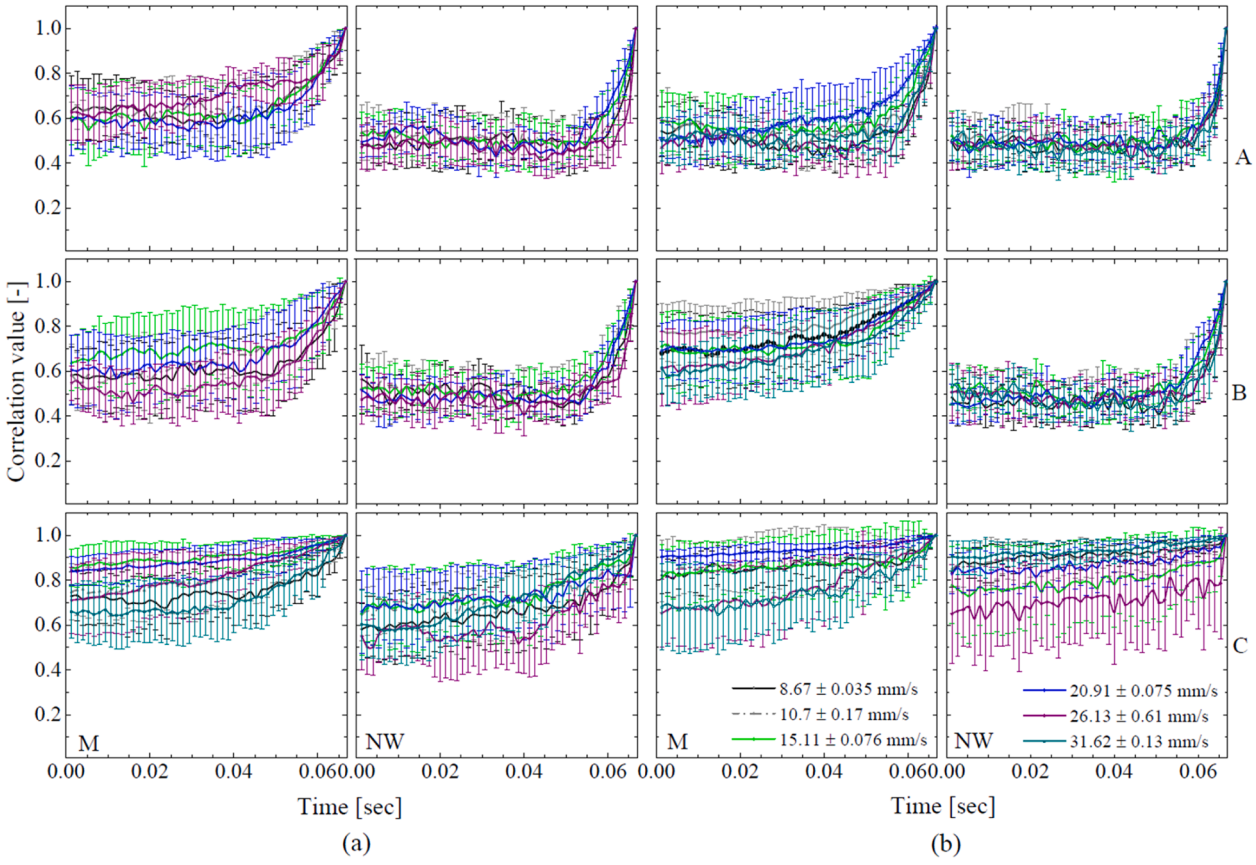

Fig. 13. Cross-correlation values of radial (a), and axial (b) gas velocity fluctuation in N_2 – water system.

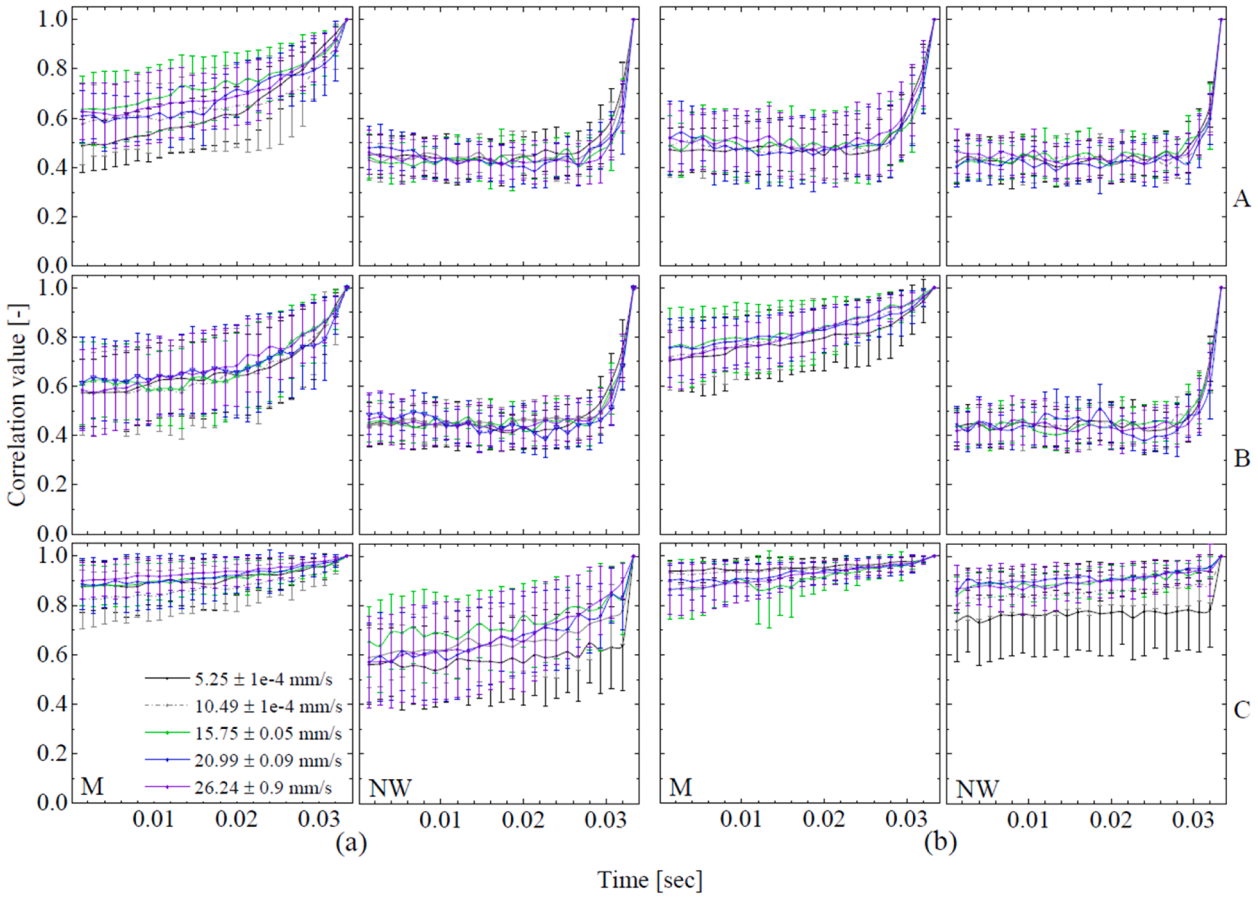

Fig. 14. Cross-correlation values of radial (a), and axial (b) gas velocity fluctuation in CO_2 – water system.

of flow dynamics. In the N_2–water system, spectra across cycles are closely aligned, especially at low frequencies, indicating consistent large-scale structures. Minor deviations at higher frequencies reflect small-scale turbulence. In contrast, the CO_2-water system shows greater cycle-to-cycle variation, particularly in near-wall regions at high U_g, due to enhanced bubble interactions and dissolution. However, this variation diminishes with column height, suggesting a shift toward uniform small-scale dynamics and reduced large-structure influence.

Figs. 12a and 12b show the power spectra of u_l' in deionized water

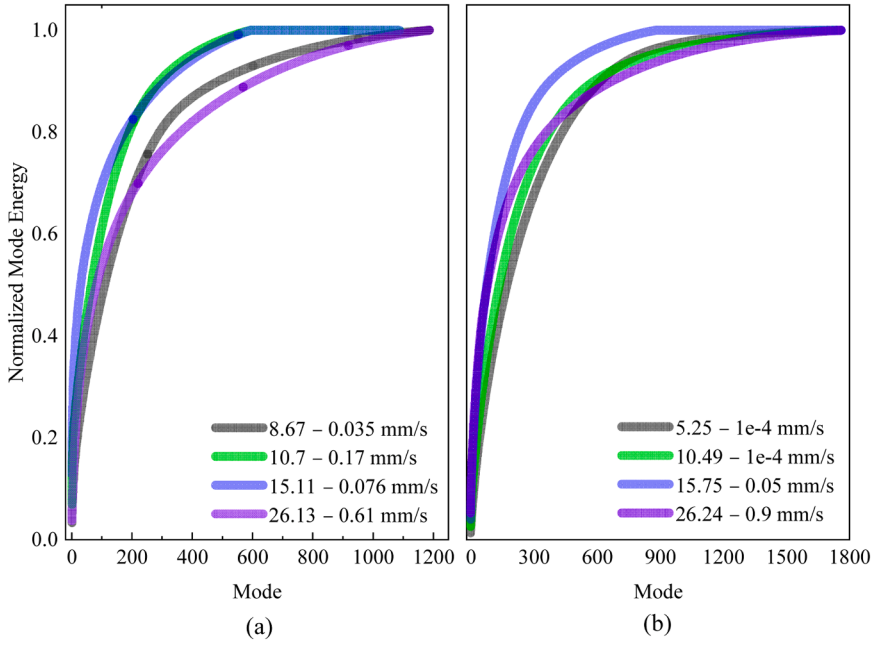

Fig. 15. Energy spectrum of velocity fluctuation of N_2 – water (a), and CO_2 – water (b) system for different gas superficial velocities.

with N_2 and CO_2 gas injected into the BCR. In the N_2-water system, the power density curves for u'_l resemble those of u'_g, with the energy spectrum in M windows remaining relatively constant for frequencies above 100 Hz. Conversely, the NW windows exhibit higher and lower spectral densities at high and low frequencies, respectively, with the M windows' curves steeper than those of NW windows. This confirms a stronger influence of small-scale fluctuations in NW windows than in M windows.

In the CO_2-water system, the power density curves for u'_l indicate that the energy spectrum is independent of frequencies below 200 Hz (approx.) for U_g between 5.25 ± 1e-4 mm/s and 26.24 ± 0.19 mm/s. Small-scale structures influence more to the energy spectrum of u'_l than that to the energy spectrum of u'_g in the CO_2-water system. With small structures contributing primarily to the energy spectra, the power density in the CO_2-water system is lower than in the N_2-water system. This absence of large-scale fluctuations is likely due to the inhibition of CO_2 bubble coalescence in water.

3.3. Cross-correlation (CC) of velocity fluctuation field

The correlation between the middle frame of a cycle and the other frames within that cycle for axial and radial u'_g in different windows for N_2 – and CO_2 – water system was calculated. CC of u'_g provides insights into the rate at which flow structures deform. A high correlation value indicates that the shape and size of flow structures change gradually, corresponding to small displacements of gas particles. Figs. 13a and 13b display the correlation value versus time curves for radial and axial u'_g in N_2-water bubbly flow. Variations in U_g do not produce a clearly

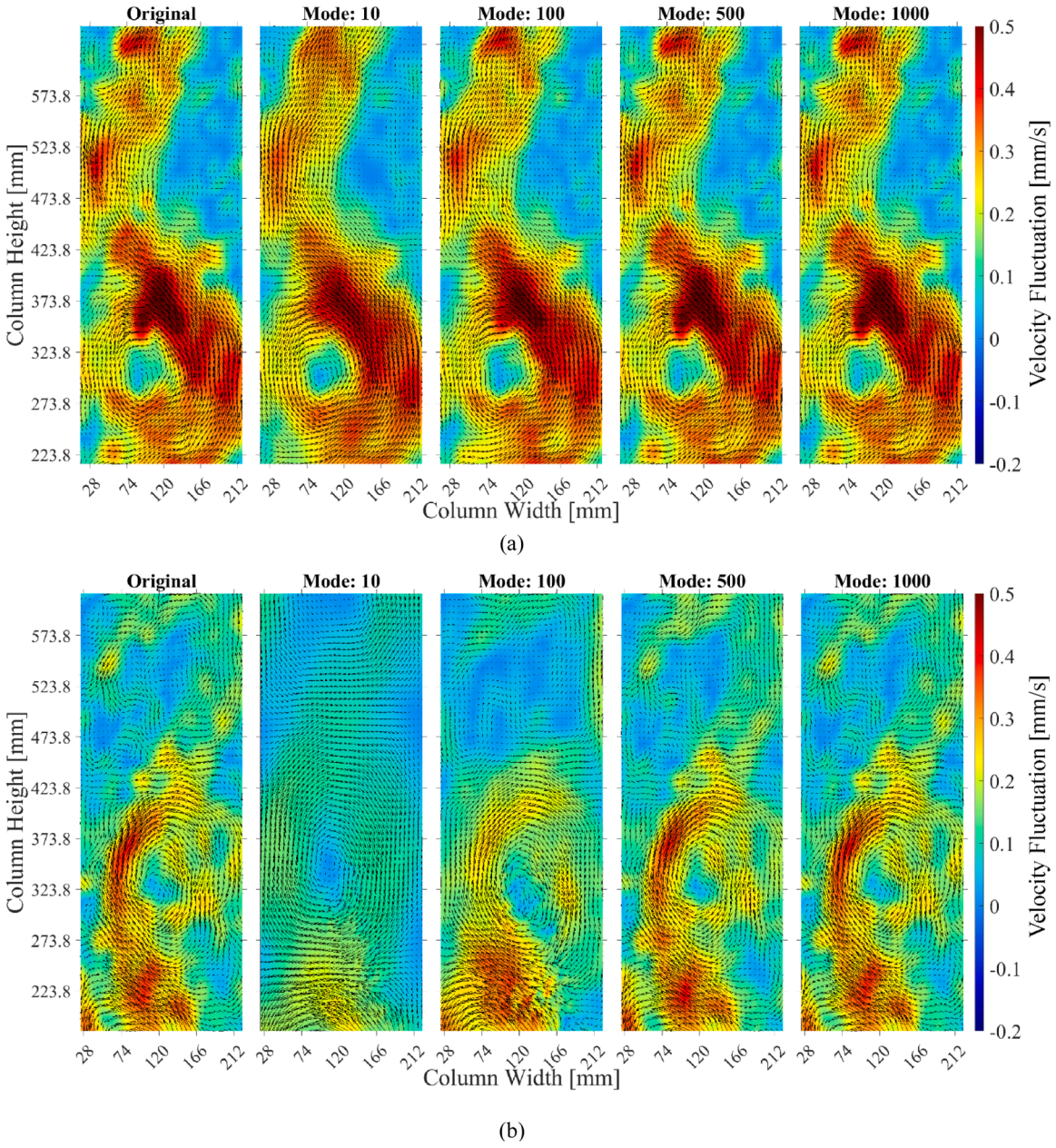

Fig. 16. Decomposition of a snapshot of N_2 – water (a), and CO_2 – water (b) gas velocity field at the gas superficial velocity of 10.7 ± 0.17 mm/s and 10.49 ± 1e-4 mm/s, respectively.

distinguishable effect on the correlation values. However, a sharp decline in correlation values is observed in the NW windows compared to the M windows. The recirculation zones near the wall consist of regions with positive and negative velocities, influenced by the central gas plume and the downward liquid velocities along the column wall. As a result, the flow field near the wall is less stable than in the center of the column. Additionally, the slope of the correlation values increases with the column height, especially in the M windows. This trend occurs because flow structures change more rapidly as they ascend against gravitational forces, with the oscillatory behavior of the bubbly flow dissipating as it rises.

The frequency of vertical movement of gas structures is less than that of horizontal movement in the CO_2-water system (Fig. 14). Therefore, a relatively slower decrease in CC values is noted for the axial gas velocity fluctuations in both N_2- and CO_2-water bubbly flows compared to the radial fluctuations. The curves imply that $\left(\frac{dCC}{dt}\right)_{M,\,CO_2} < \left(\frac{dCC}{dt}\right)_{M,\,N_2}$ and $\left(\frac{dCC}{dt}\right)_{NW,\,CO_2} > \left(\frac{dCC}{dt}\right)_{NW,\,N_2}$ for the first 0.03 sec. These results indicate that the recirculation zones of the CO_2-water bubbly flow and central regions of the N_2-water bubbly flow exhibit more rapid structural changes.

3.4. Characterization of velocity fluctuation field by decomposition

SVD allows the identification of flow structures and their relative energy contributions. All frames from each experimental condition are sequentially compiled to perform decomposition on the vector field. Fig. 15 illustrates the normalized cumulative energy content as a function of mode number across various gas superficial velocities. Each

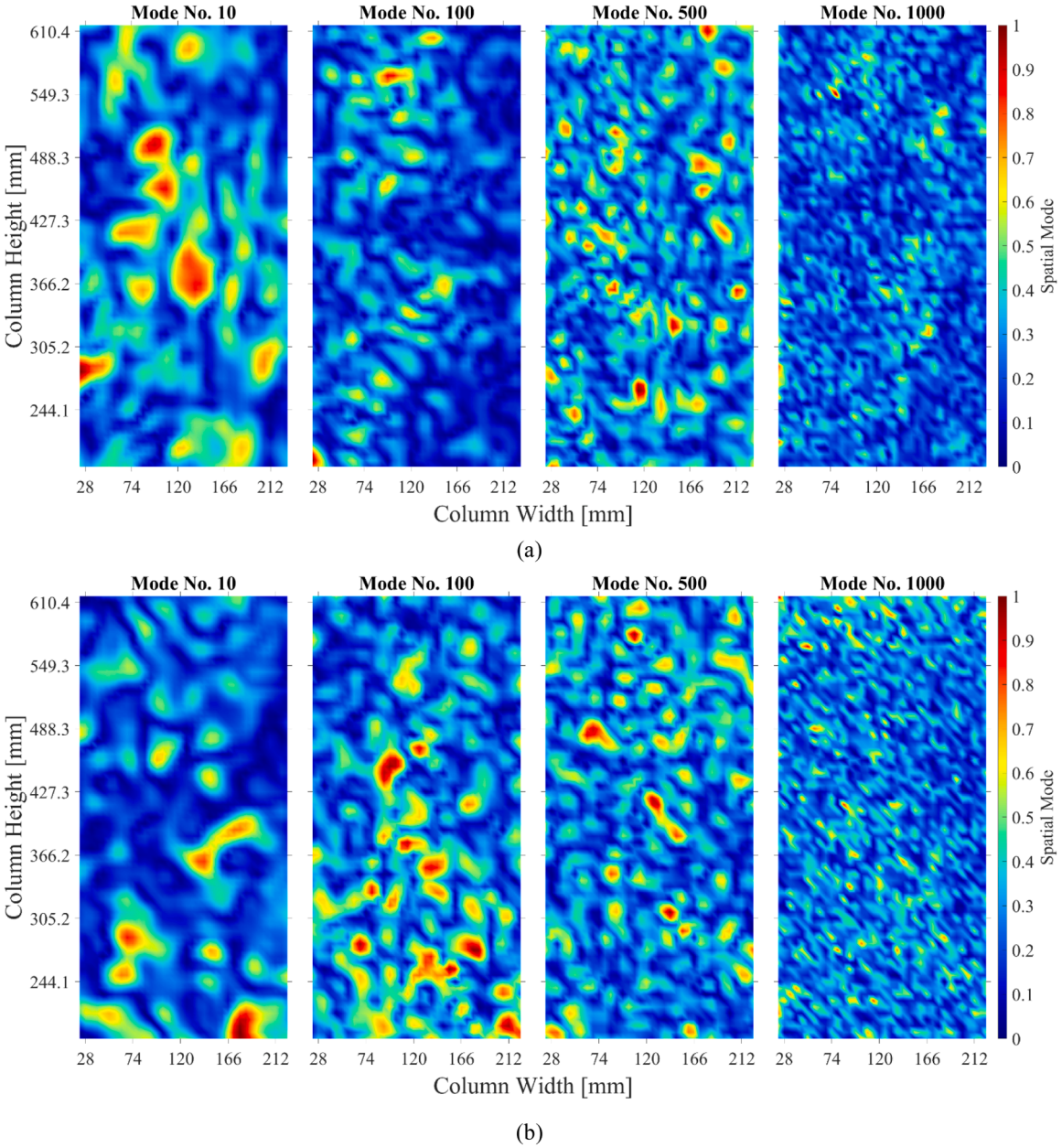

Fig. 17. Distribution of spatial modes of N_2 – water (a), and CO_2 – water (b) gas velocity field at the gas superficial velocity of 20.91 ± 0.075 mm/s and 20.99 ± 0.09 mm/s, respectively.

experimental snapshot corresponds to a mode number. For the N_2 –water and CO_2 –water systems, 1200 (100 frames × 12 cycles) and 1800 frames (50 frames × 36 cycles) were captured, respectively, resulting in maximum mode numbers of 1200 and 1800. Thus, the horizontal axis lengths differ. As the mode number increases, the normalized mode energy rises sharply at first and then gradually plateaus toward unity. Interestingly, both the lowest and highest values of U_g require a greater number of modes to capture the majority of the energy content and intermediate velocities contain more energy than the lowest and the highest U_gs. Specifically, the first 850 modes account for at least 95 % and 93 % of the total kinetic energy in N_2-water and CO_2-water bubbly flows, respectively. This behavior highlights the correlation between increased superficial velocity and stronger mode dominance, likely associated with more pronounced flow features or reduced stochasticity in the system.

Fig. 16 illustrates the flow structures corresponding to the velocity fluctuation field at $U_g \approx 10.5$ mm/s across multiple modes, with modal energy distributions given in Fig. 15. At this velocity, the first 100 modes account for 61 % and 41 % of the total kinetic energy in N_2-water and CO_2-water flows, respectively, capturing primarily large-scale fluctuations. The dominant structures correspond to recirculation zones, most pronounced in the mid-column region (≈ 223–423 mm), where vortex cores are clearly resolved.

The spectral analysis (Figs. 11–12) complements this view: N_2–water retains energy in large scales, while CO_2-water exhibits pronounced small-scale contributions. In Fig. 16, low-order modes (e.g., mode 10) isolate the largest vortical structures; in CO_2-water these appear diffuse and bottom-localized, consistent with energy dispersion and dissolution-induced weakening of coherent circulation. In contrast, N_2–water shows column-spanning, well-organized lobes. By mode 100, N_2–water retains coherent recirculation augmented by shear-layer perturbations, whereas CO_2-water already develops multiple small vortices and tilted streaks, evidencing early onset of asymmetry and micro-mixing. At mode 500, N_2–water displays fine-scale fluctuations superimposed on dominant lobes, while CO_2-water becomes highly fragmented, with numerous dispersed vortices reflecting intensified small-scale turbulence. At mode 1000, both systems reconstruct the original fields with high fidelity, but the CO_2 case requires more modes to capture its inherently finer-scale dynamics driven by dissolution and interfacial effects. These trends are consistent with Aranyi et al (Arányi et al., 2013)., who reported that low modes contain most of the energy and represent large-scale flow, while finer structures progressively emerge at higher modes.

The spatial mode contours in Fig. 17 corroborates these observations. In N_2-water (Fig. 17a), modes 10 and 100 form vertically continuous, symmetric lobes centered on the plume, characteristic of column-wide recirculation. Mode 100 introduces lateral streaks along the plume edge, reflecting shear-layer meandering, but the structures remain vertically uniform. Higher modes (500, 1000) fragment into rounded, isotropic patches near the plume core and interface, attributable to localized bubble wakes and the dissipative tail of inert-gas turbulence—consistent with poor N_2 solubility sustaining large-scale circulation and concentrating energy in low modes. By contrast, the CO_2–water column (Fig. 17b) shows attenuated, bottom-localized lobes at mode 10, with mode 100 producing irregular, tilted streaks indicative of plume thinning and dissolution-driven asymmetry. At higher orders (500, 1000), numerous elongated, vertically aligned streaks dominate, evidencing persistent anisotropy in the fine-scale field. This redistribution of energy toward finer, vertically asymmetric structures reflects the high solubility of CO_2, where bubble shrinkage, suppressed coalescence, and enhanced interfacial area shift the flow regime from plume-scale recirculation toward dissolution-enhanced micro-mixing.

4. Conclusion

A detailed understanding of multiphase flow hydrodynamics in BCRs is essential for improving their efficiency in various industrial applications. The comparative effects of dissolving and non-dissolving bubbles on the velocity field and flow patterns are yet to be fully clarified. Additionally, separating gas and liquid phases poses challenges due to light interference and shadows. This study addresses these aspects using imaging, image-processing, and reconstruction methods. A synchronized PIV and BIV technique captured liquid and gas velocities with a 0.133 ms time lag between consecutive frames. Ensemble averaging of the velocity fields recovered data lost in shadowed areas, and distorted velocity field locations were reconstructed, resulting in uncertainties with an RMSE of less than 0.1.

i. In the N_2-water system, u'_g and u'_l exhibit a unimodal distribution at $U_g = 8.67 \pm 0.035$ mm/s and for $U_g > 20.91 \pm 0.075$ mm/s. In contrast, the CO_2-water system shows a unimodal distribution at higher velocities (15.75 ± 0.05 mm/s to 26.24 ± 0.09 mm/s). The distribution changes from unimodal to bimodal at intermediate velocities (8.67 ± 0.035 mm/s > U_g < 20.91 ± 0.075 mm/s) in the N_2-water system, and at lower velocities (5.25 ± 1e-4 mm/s and 10.49 ±1e-4 mm/s) in the CO_2-water system. The bimodal distribution results from bubble interactions and dissolution.
ii. The power spectrum indicates the energy content of small and large structures in the bubbly flows. Large structures generally contribute more energy in center regions. In the CO_2 bubbly flows, energy density remains constant near the walls of BCRs. The A-NW windows of CO_2-water systems exhibit the highest energy due to velocity fluctuations.
iii. U_g does not significantly impact the temporal evolution of cross-correlation (CC). Flow structures in the NW windows change faster than those in the M windows. The key relationships related to CC are: $\frac{dCC}{dt} \propto column\ height$, $\left(\frac{dCC}{dt}\right)_M < \left(\frac{dCC}{dt}\right)_{NW}$, $\left(\frac{dCC}{dt}\right)_{M,\,CO_2} > \left(\frac{dCC}{dt}\right)_{NW,\,N_2}$, and $\left(\frac{dCC}{dt}\right)_{NW,\,CO_2} > \left(\frac{dCC}{dt}\right)_{NW,\,N_2}$.
iv. Flow pattern and energy content were analyzed using SVD. The CO_2-water system exhibited a higher number of small structures than the N_2-water system. Both large and small structures contribute significantly to the overall energy.

The findings from various methods are qualitatively consistent and provide valuable insights for developing numerical models and designing more efficient BCRs. Future studies could explore different combinations of N_2- and CO_2 gas plumes to assess the impact of bubble dissolution on flow patterns.

CRediT authorship contribution statement

D. Sarker: Visualization, Investigation, Data Analysis, Writing-Original draft preparation, Reviewing and editing. **C. V. Schinkel:** Visualization, Writing- Reviewing and editing. **L. M. Portela:** Conceptualization, Fund securing, Supervision.

Declaration of Competing Interest

The authors declare that there are no known competing interests that could have appeared to influence the results reported in this article.

Acknowledgments

The authors gratefully acknowledge the Netherlands Organisation for Scientific Research (NWO) for the financial support of this study.

Appendix

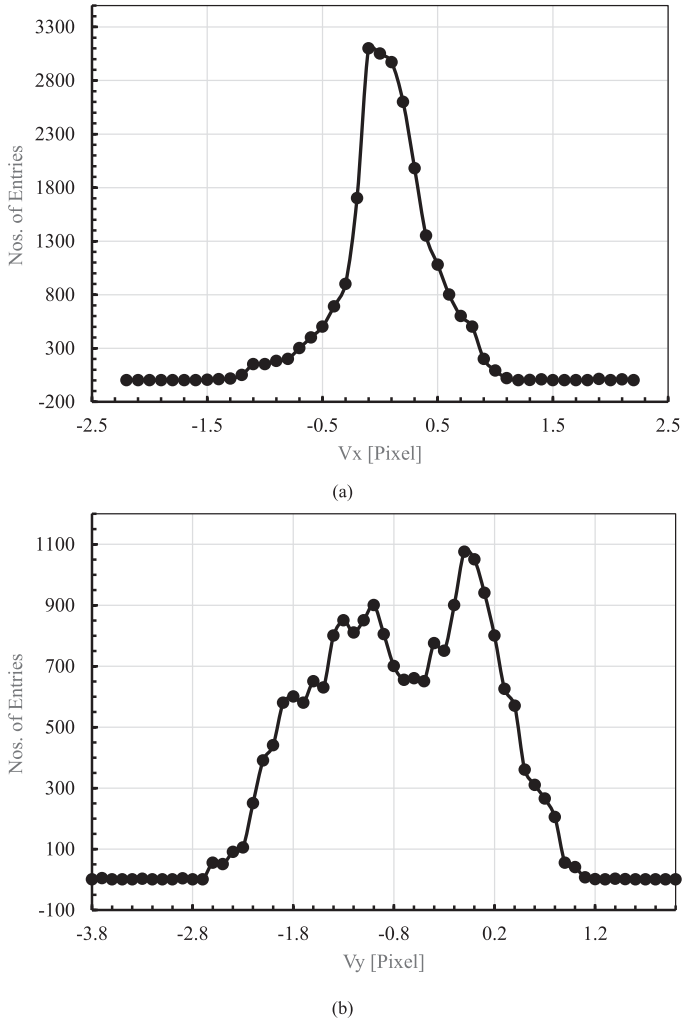

Fig. A1. PDF showing pixel shift of velocity vectors in X (a) and Y (b) directions

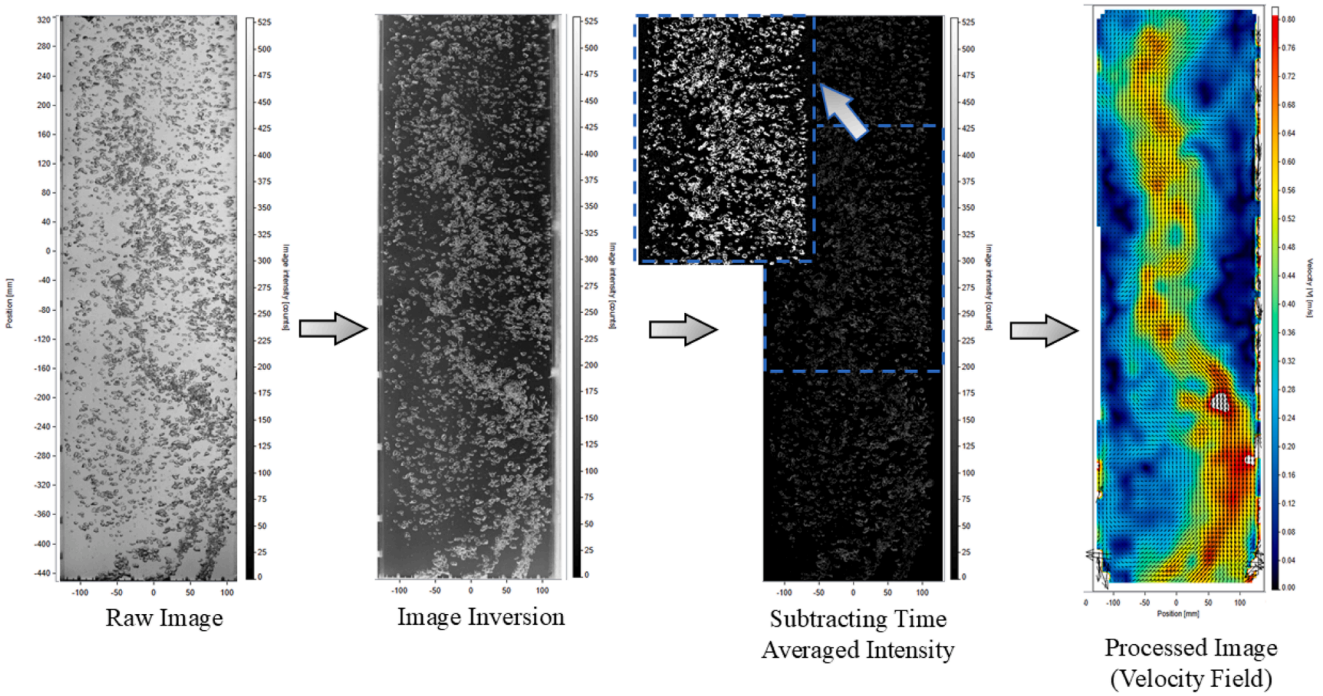

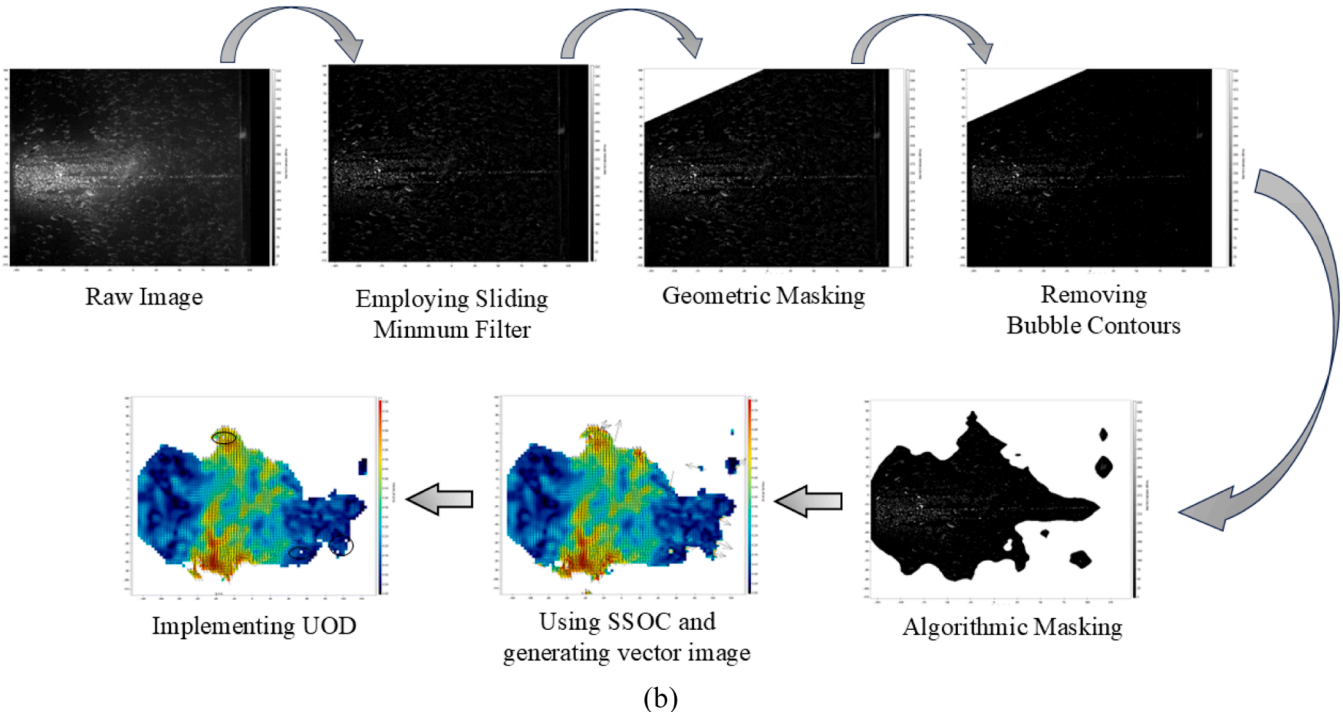

Fig. A2. Image processing steps for BIV (a) and PIV (b)

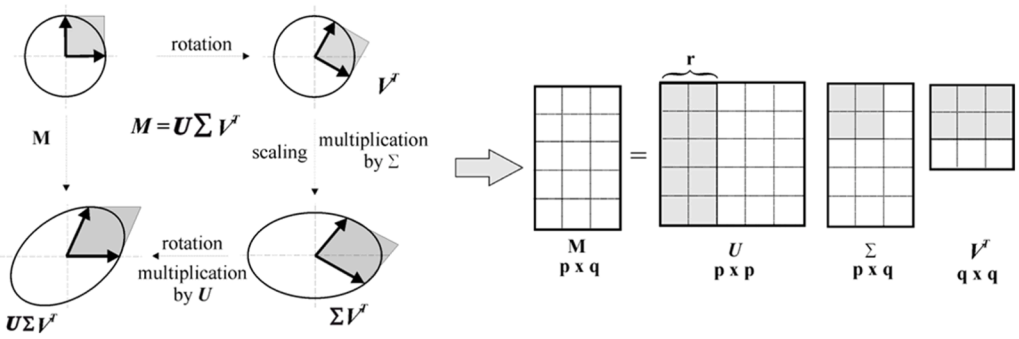

Fig. A3. A schematic of SVD principle

References

Kantarci, N., Borak, F., Ulgen, K.O., 2005. Bubble column reactors. Process Biochem. 40, 2263–2283. https://doi.org/10.1016/j.procbio.2004.10.004.

S. Lefebvre, C. Guy, Characterization of bubble column hydrodynamics with local measurements, 1999.

Delnoij, E., Kuipers, J.A.M., Van Swaaij, W.P.M., Westerweel, J., 2000. Measurement of gas-liquid two-phase flow in bubble columns using ensemble correlation PIV. Chem. Eng. Sci. 55.

N.S. Panicker, Computational models for turbulent bubbly flows in bubble columns, 2017.

Medjiade, W.T., Rosenbaum, A.A., Schumpe, A., 2017. Flow regime transitions in a bubble column. Chem. Eng. Sci. 170. https://doi.org/10.1016/j.ces.2017.04.010.

Sarker, D., Schinkel, C.V., Portela, L.M., 2023. Effect of N2 and CO2 bubbles on gas volume fraction and flow pattern in a quasi-2D bubble column by shadow imaging. Chem. Eng. Res. Des. 189, 500–515. https://doi.org/10.1016/j.cherd.2022.11.032.

Mudde, R.F., Lee, D.J., Reese, J., Fan, L.-S., 1997a. Role of coherent structures on reynolds stresses in a 2-D bubble column. Am. Inst. Chem. Eng. J. 43, 913–926.

Raimundo, P.M., Cloupet, A., Cartellier, A., Beneventi, D., Augier, F., 2019. Hydrodynamics and scale-up of bubble columns in the heterogeneous regime: Comparison of bubble size, gas holdup and liquid velocity measured in 4 bubble columns from 0.15 m to 3 m in diameter. Chem. Eng. Sci. 198, 52–61.

Besagni, G., Varallo, N., Mereu, R., 2023. Computational Fluid Dynamics Modelling of Two-Phase Bubble Columns: A Comprehensive Review. Fluids 8. https://doi.org/10.3390/fluids8030091.

F. Durst, A.M.K.P. Taylor, J.H. Whitelaw, Experimental and numerical investigation of bubble-driven laminar flow in an axisymmetric vessel, 1984.

Besbes, S., El Hajem, M., Ben Aissia, H., Champagne, J.Y., Jay, J., 2015. PIV measurements and Eulerian-Lagrangian simulations of the unsteady gas-liquid flow in a needle sparger rectangular bubble column. Chem. Eng. Sci. 126, 560–572. https://doi.org/10.1016/j.ces.2014.12.046.

Cerqueira, R.F.L., Paladino, E.E., Ynumaru, B.K., Maliska, C.R., 2018a. Image processing techniques for the measurement of two-phase bubbly pipe flows using particle image and tracking velocimetry (PIV/PTV). Chem. Eng. Sci. 189, 1–23. https://doi.org/10.1016/j.ces.2018.05.029.

Alméras, E., Cazin, S., Roig, V., Risso, F., Augier, F., Plais, C., 2016. Time-resolved measurement of concentration fluctuations in a confined bubbly flow by LIF. Int. J. Multiph. Flow. 83, 153–161. https://doi.org/10.1016/j.ijmultiphaseflow.2016.03.011.

Risso, F., 2018. Agitation, mixing, and transfers induced by bubbles. Annu Rev. Fluid Mech. 50, 25–48.

Zamansky, R., Roy De Bonneville, F.Le, Risso, F., 2024. Turbulence induced by a swarm of rising bubbles from coarse-grained simulations. J. Fluid Mech. 984.

Prakash, V.N., Martínez Mercado, J., Van Wijngaarden, L., Mancilla, E., Tagawa, Y., Lohse, D., Sun, C., 2016. Energy spectra in turbulent bubbly flows. J. Fluid Mech. 791, 174–190. https://doi.org/10.1017/jfm.2016.49.

Risso, F., 2019. Bubble-Induced Turbulence. In: Gorokhovski, M., Godeferd, F.S. (Eds.), Turbulent Cascades II. Springer International Publishing, Cham, pp. 189–196.

Ruiz-Rus, J., Ern, P., Roig, V., Martínez-Bazán, C., 2022. Coalescence of bubbles in a high Reynolds number confined swarm. J. Fluid Mech. 944. https://doi.org/10.1017/jfm.2022.492.

Long, S., Yang, X., Yang, J., Sommerfeld, M., 2022. Euler/Euler large eddy simulation of bubbly flow in bubble columns under CO2 chemisorption conditions. Chem. Eng. J. 445. https://doi.org/10.1016/j.cej.2022.136654.

Leonard, C., Ferrasse, J.H., Lefevre, S., Viand, A., Boutin, O., 2021. Bubble rising velocity and bubble size distribution in columns at high pressure and temperature: From lab scale experiments to design parameters. Chem. Eng. Res. Des. 173, 108–118. https://doi.org/10.1016/j.cherd.2021.07.003.

Hosen, H.F., Ozan, S.C., Jakobsen, H.A., 2022. On the coalescence of dissolving bubbles in surfactant presence. Int. J. Multiph. Flow. 148. https://doi.org/10.1016/j.ijmultiphaseflow.2021.103919.

Lau, Y.M., Hampel, U., Schubert, M., 2018. Ultrafast X-ray tomographic imaging of multiphase flow in bubble columns - Part 1: Image processing and reconstruction comparison. Int. J. Multiph. Flow. 104, 258–271. https://doi.org/10.1016/j.ijmultiphaseflow.2018.02.010.

Cerqueira, R.F.L., Paladino, E.E., Ynumaru, B.K., Maliska, C.R., 2018b. Image processing techniques for the measurement of two-phase bubbly pipe flows using particle image and tracking velocimetry (PIV / PTV). Chem. Eng. Sci. 189, 1–23. https://doi.org/10.1016/j.ces.2018.05.029.

Liu, Y., Zhang, L., Zhou, L., 2020. Development of modeling and simulation of bubble-liquid hydrodynamics in bubble column. Energy Sci. Eng. 8, 327–339. https://doi.org/10.1002/ese3.487.

Seyfi, S., Karimpour, S., Balachandar, R., 2024. Simultaneous flow and particle measurements for multiphase flows in hydraulic engineering: A review and synthesis of current state. Flow. Meas. Instrum. 99. https://doi.org/10.1016/j.flowmeasinst.2024.102666.

Scharnowski, S., Kähler, C.J., 2020. Particle image velocimetry - Classical operating rules from today's perspective. Opt. Lasers Eng. 135. https://doi.org/10.1016/j.optlaseng.2020.106185.

Bröder, D., Sommerfeld, M., 2002. An advanced LIF-PLV system for analysing the hydrodynamics in a laboratory bubble column at higher void fractions. Exp. Fluids 33, 826–837. https://doi.org/10.1007/s00348-002-0502-z.

B.Ralph Lindken, L. Gui, W. Merzkirch, Velocity Measurements in Multiphase Flow by Means of Particle Image Velocimetry, 1999.

Kim, M., Lee, J.H., Park, H., 2016a. Study of bubble-induced turbulence in upward laminar bubbly pipe flows measured with a two-phase particle image velocimetry. Exp. Fluids 57. https://doi.org/10.1007/s00348-016-2144-6.

A. Tokuhiro, M. Maekawa, K. Iizuka, K. Hishida, M. Maeda, Turbulent ¯ow past a bubble and an ellipsoid using shadow-image and PIV techniques PERGAMON, 1998.

E. Carpintero-Rogero, B. Kröss, T. Sattelmayer, Simultaneous HS-PIV and shadowgraph measurements of gas-liquid flows in a horizontal pipe, 2006.

Sathe, M.J., Thaker, I.H., Strand, T.E., Joshi, J.B., 2010. Advanced PIV/LIF and shadowgraphy system to visualize flow structure in two-phase bubbly flows. Chem. Eng. Sci. 65, 2431–2442. https://doi.org/10.1016/j.ces.2009.11.014.

Siddiqui, M.I., Munir, S., Heikal, M.R., de Sercey, G., Aziz, A.R.A., Dass, S.C., 2016. Simultaneous velocity measurements and the coupling effect of the liquid and gas phases in slug flow using PIV–LIF technique. J. Vis. (Tokyo) 19, 103–114. https://doi.org/10.1007/s12650-015-0302-1.

Kim, M., Lee, J.H., Park, H., 2016b. Study of bubble-induced turbulence in upward laminar bubbly pipe flows measured with a two-phase particle image velocimetry. Exp. Fluids 57. https://doi.org/10.1007/s00348-016-2144-6.

Elhimer, M., Praud, O., Marchal, M., Cazin, S., Bazile, R., 2017. Simultaneous PIV/PTV velocimetry technique in a turbulent particle-laden flow. J. Vis. (Tokyo) 20, 289–304. https://doi.org/10.1007/s12650-016-0397-z.

Kováts, P., Thévenin, D., Zähringer, K., 2018. Characterizing fluid dynamics in a bubble column aimed for the determination of reactive mass transfer. Heat. Mass Transf. 54, 453–461.

Yan, X., Yao, Y., Meng, S., Zhao, S., Wang, L., Zhang, H., Cao, Y., 2021. Comprehensive particle image velocimetry measurement and numerical model validations on the gas–liquid flow field in a lab-scale cyclonic flotation column. Chem. Eng. Res. Des. 174, 1–10. https://doi.org/10.1016/j.cherd.2021.07.024.

Sommer, A.E., Draw, M., Wang, L., Schmidtpeter, J., Hessenkemper, H., Gatter, J., Nam, H., Eckert, K., Rzehak, R., 2023. Hydrodynamics in a Bubble Column – Part 1: Two-Phase Flow. Chem. Eng. Technol. 46, 1763–1772. https://doi.org/10.1002/ceat.202300130.

Chen, W., Huang, G., Hu, Y., Song, Y., Yin, J., Wang, D., 2024. Two-Phase Stereo-PIV measurement techniques for Gas-Liquid Two-Phase flow — Methodology and validation. Chem. Eng. Sci. 288. https://doi.org/10.1016/j.ces.2024.119787.

W.-D. Deckwer', A. Schumpe, IMPROVED TOOLS FOR BUBBLE COLUMN REACTOR DESIGN AND SCALE-UP, 1993.

Mudde, R.F., Lee, D.J., Reese, J., Fan, L.-S., 1997b. Role of coherent structures on reynolds stresses in a 2-D bubble column. Am. Inst. Chem. Eng. J. 43, 913–926.

Lumley, J.L., 1967. The structure of inhomogeneous turbulent flows. Atmos. Turbul. Radio Wave Propag. 166–178.

de Lamotte, A., Delafosse, A., Calvo, S., Toye, D., 2018. Analysis of PIV measurements using modal decomposition techniques, POD and DMD, to study flow structures and

their dynamics within a stirred-tank reactor. Chem. Eng. Sci. 178, 348–366. https://doi.org/10.1016/j.ces.2017.12.047.

Yin, S., Fan, Y., Sandberg, M., Li, Y., 2019. PIV based POD analysis of coherent structures in flow patterns generated by triple interacting buoyant plumes. Build. Environ. 158, 165–181. https://doi.org/10.1016/j.buildenv.2019.04.055.

Xu, Y., Wang, X., Wang, F., Song, B., Zhang, Y., Shi, C., 2020. Quantitative analysis of coherent structures affecting instantaneous fluctuation of point-source plumes based on PIV-POD method. Energy Built Environ. 1, 131–138. https://doi.org/10.1016/j.enbenv.2019.11.004.

Munir, S., Siddiqui, M.I., Heikal, M., Abdul Aziz, A.R., de Sercey, G., 2015. Identification of dominant structures and their flow dynamics in the turbulent two-phase flow using POD technique. J. Mech. Sci. Technol. 29, 4701–4710. https://doi.org/10.1007/s12206-015-1017-x.

Deshpande, S.S., Tabib, M.V., Joshi, J.B., Kumar, V.R., Kulkarni, B.D., 2010. Analysis of flow structures and energy spectra in chemical process equipment. J. Turbul. 11, N5. https://doi.org/10.1080/14685241003662668.

Arányi, P., Janiga, G., Zähringer, K., Thévenin, D., 2013. Analysis of different POD methods for PIV-measurements in complex unsteady flows. Int J. Heat. Fluid Flow. 43, 204–211. https://doi.org/10.1016/j.ijheatfluidflow.2013.07.001.